Monthly Notices of the ROYAL ASTRONOMICAL SOCIETY

MNRAS **516,** 2757–2774 (2022) https://doi.org/10.1093/mnras/stac2310
Advance Access publication 2022 August 18

Underexpanded gas jets of Mach 2: the changing physical structure and power transmission

Michael D. Smith★ and Thomas L. R. Keogh
Centre for Astrophysics & Planetary Science, The University of Kent, Canterbury Kent CT2 7NH, UK

Accepted 2022 August 14. Received 2022 August 14; in original form 2022 May 23

ABSTRACT

Supersonic jets with excess gas pressure are associated with many phenomena including radio galaxies, protostars, volcanic plumes, rocket exhausts, and champagne cork popping. Some common properties are derived here based on steady uniform hydrodynamic flow from a circular orifice. We present a systematic numerical study over a wide range of parameters for Mach 2 jets, concentrating on simulations of jets with pressures exceeding the ambient pressure. With cylindrical symmetry, we show how the location of the stand-off and following downstream shocks depend not only on the overpressure but also on the density due to a feedback loop, which results in an oscillatory flow pattern. We conclude that rapidly varying and gradually evolving shock patterns arise even from steady uniform jets. This can take the form of turbulent plumes at high overpressures and regular oscillations at low overpressures. We identify where this screeching contributes to noise and sound wave generation, which may aid the regulation of star and galaxy formation. However, the main effect for such low Mach number jets is to drive a circulatory motion in which the ambient medium is driven out along the axial direction while mass and energy flow laterally inwards, setting up a large advection pattern. Once the initial bow shock has propagated out, the noise from the jet is insufficient to significantly alter the environment. High Mach number jets do not follow these conclusions and will be treated separately.

Key words: hydrodynamics.

1 INTRODUCTION

Gas is able to propagate away from a vast range of objects in astrophysics and space science in the form of collimated supersonic jets (Smith 2012). Examples of note were associated with comet 67P on approach to the inner Solar system (Vincent et al. 2016) and within the plumes of the moon Enceladus (Hansen et al. 2008). Further afield, spectacular jets of shocked molecules are streaming away from the protostar associated with HH 212 (Smith, O'Connell & Davis 2007) and from deep within the M87 galaxy, launched from the vicinity of a supermassive black hole (Perlman et al. 2001). Due to the release of bottled-up pressures, jets are also studied for reasons of industrial and domestic safety (Franquet et al. 2015; Liger-Belair, Cordier & Georges 2019).

When resolved, in time or space, bright compact knots are revealed that can be spatially fixed or rapidly moving away from the driving source (Buehrke, Mundt & Ray 1988; Derlopa et al. 2019; Massi et al. 2022). The knots are associated with shock waves since shock fronts are locations where particle acceleration and excitation are likely to be greatly enhanced through rapid compression and heating (Meyer et al. 2016).

Early laboratory studies of supersonic gas jets were in response to the need to model the motion of rockets through the atmosphere (Adamson & Nicholls 1959; Carlson & Lewis 1964). Rocket exhausts are formed through the release of high-pressure gas with the excess pressure leading to a diverging and converging pattern downstream. Oblique shock waves occur in the flow with strong transverse shocks within the converging section. This scenario is sketched in Fig. 1 and provides the starting point for this numerical study.

The early studies were limited in scope by their experimental nature. The analysis through the method of characteristics is also of limited value because of the approximations needed to cope with the flow downstream of the shocks and the rotation introduced into the flow by the curved shock fronts. However, work has continued in specific directions of interest such as the production of jet screeching and noise. Numerical studies such as by Norman et al. (1982) were independently inspired by interferometric maps of radio galaxies and their modelling in terms of de Laval nozzles (Blandford & Rees 1974). Most early simulations assumed a pressure-matched supersonic propagation in which the exit jet pressure was equated to the ambient pressure.

Under-pressured supersonic jets are those in which the jet pressure at the nozzle is lower than the ambient pressure. Shock waves can develop before the exit at the nozzle as the flow pressure attempts to adjust. This flow separation is most likely in rocket exhausts near take-off since atmospheric pressure is relatively high at ground level. The flow separation within the nozzle leads to the rapid development of turbulence therein (Daviller et al. 2020).

Over-pressured jets, on the other hand, are important shock generators that can be particularly relevant in the vicinity of astrophysical objects, where the jets propagate away from the cores that harbour protostars or supermassive black holes. As a jet exits from the core, the steep negative pressure gradient in the ambient medium (Smith 1982; Porth & Komissarov 2015) leaves the jet pressure relatively high at the effective exit of the core.

The situation does of course become reversed downstream, once the jet has expanded. The pressure on the jet axis continues to fall

★ E-mail: m.d.smith@kent.ac.uk

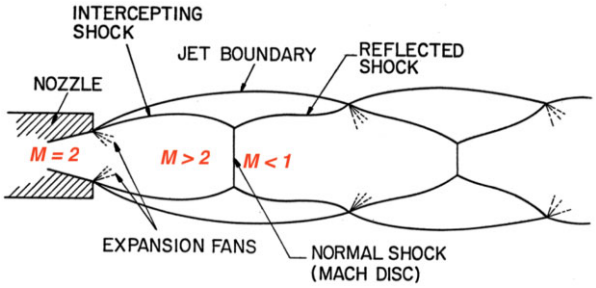

Figure 1. A sketch of the flow pattern in an underexpanded/overpressured jet. Taken and modified from Adamson & Nicholls (1959).

oblivious of the surface pressure. Hence, the pressure gradient across the flow is reversed and the flow converges. As shown in Fig. 1, a shock on the axis is then necessary to then raise the pressure back up. This delay in communication between the surface and axis causes a hysteresis effect that can also cause oscillatory instabilities through positive feedback.

A comprehensive investigation of underexpanded jets remains to be performed, as noted by Franquet et al. (2015). This can now be rectified through numerical simulations. The distance of the first shock from the nozzle, termed the stand-off distance, provides a direct measure of flow parameters. The early experimental studies derived a relationship between this distance and the jet overpressure and Mach number, which suggests that the stand-off distance may characterize the underlying flow (Carlson & Lewis 1964; Davidor & Penner 1971). However, only high overpressures and low Mach numbers were studied. We investigate this here to determine if the previous relationship extends to a general result.

In the process, we recover the result that not all flows approach a steady pattern and that the ambient density plays a role in determining the flow time from the stand-off shock to the nozzle exit. Thus, although we do not drive pulses into the jet in this first work, we do consider long-term, non-turbulent variability. This can lead to screeching and crackling noise as energy propagates transversely into the ambient medium.

We simulate here hydrodynamic supersonic jets. The jets consist of a uniform adiabatic gas that is inserted on the boundary of a cylindrical grid. We assume cylindrical symmetry that may be justified close to the orifice while the growth of surface instabilities remains small. We consider appropriate ranges in pressure and density ratios between the two media and test analytical approximations.

Note also that the jet is inviscid. The slip condition applies at the interface between the jet and ambient medium where a narrow viscous boundary layer separates the two inviscid flows. At the tip of the nozzle, a high-pressure gradient acts to bend the jet flow as described by a Prandtl–Meyer expansion fan.

The pressure ratio referred to here is the initial pressure ratio. We take steps to allow the ambient pressure to relax by taking a simulation domain extending to 65×130 jet radii and ramping up the initial jet velocity to avoid blowing the ambient medium off the domain.

It should be remarked that the ambient medium is generally not uniform and may contain long-lived vortices on small scales and significant pressure variations are allowed to develop. This contrasts with the steady-state uniform pressure conditions in analytical solutions for which the ambient density plays no role. In real flows, the density is important since it provides the inertia that determines the potential for feedback mechanisms to operate.

One motivation here is to determine how the details of the flow pattern can provide information on the driving source. In particular, the location of the stand-off shock on the jet axis provides a quantitative measure. Comparison is also achieved by studying cross-sections of the physical variables at specific times and space–time diagrams of the pressure along the jet axis. Moreover, we calculate how the energy is shared out along the jet and how much is dispersed.

A second motivation is to relate the shocks to those responsible for the emission from distant astrophysical jets. This analysis may only lay the foundations for such a comparison, since additional physics will need to be incorporated. This includes cooling, particle acceleration, and chemical processes as well as the magnetic field, gravitational, and relativistic effects. In the aerodynamic context, the flow of the external medium over the jet engine during flight will alter the feedback around the exhausting jet. Early results downplayed the influence (Buckley 1975) unless the free-stream Mach number is itself high.

Many simulations of overpressured jets have already been performed and analysed (e.g. Gómez et al. 1997; Martí, Perucho & Gómez 2016; Moya-Torregrosa et al. 2021). These works suggest that the flow patterns and shock configurations may be relevant to those associated with active galactic nuclei. However, specific conditions were chosen and parameter space not explored. For example, Mizuno et al. (2015) studied the magnetic field topology. They began all simulations with a pre-existing jet, single values of density, a Mach number of 1.69, and a pressure ratio of 1.5. Hence, although the simulations indicate how the field may influence a flow pattern, it is not clear how the results would differ in other circumstances. In particular, Mizuno et al. (2015) note that the dependence on the pressure ratio remains to be investigated. In contrast, we ignore the magnetic field but consider wide ranges of density, Mach number and pressure and show that the resulting flow pattern depends crucially on these choices.

In a subsequent study, we will consider a full range of Mach numbers. We will superimpose dynamical and geometric factors while maintaining this two-dimensional approach. In particular, we intend to consider the influence of velocity shear and spray (fixed non-zero opening angle. Then we wish to superimpose velocity and density pulsations and bursts, motivated by the proper motions of knots that are difficult to explain within the steady inflow context. In addition, the nozzle we model in astrophysical jets may vary in the opening angle, since the opening may be itself determined by the jet origin or even tidal forces.

2 METHOD

2.1 The code

We evolve the equations of hydrodynamics in 2D axisymmetry. The simulations were performed with PLUTO, a grid-based code, incorporating Godunov-type shock-capturing schemes, which is freely distributed (Mignone et al. 2007).[1] After comparing the results of numerous options, we chose a fast linear interpolation time-stepping (denoted HLLC) Riemann solver as developed by Harten, Lax, and Van Leer and detailed by Toro, Spruce & Speares (1994). The Hancock time-stepping Courant–Friedrichs–Lewy number is taken as 0.4.

The subsequent post-processing was performed with IDL software.

[1] http://plutocode.ph.unito.it/.

Table 1. The general initial conditions for the non-dimensional parameters and their example scaled interpretations taking both a light and heavy jet.

–	–	Light jet unit value	Heavy jet unit value	Rocket exhaust	FR I radio galaxy
Jet radius	$r_{\rm jet}$	1	1	13.5 cm	2.5 kpc
Simulated length	D	30	30	405 cm	75.0 kpc
Mach number	$M_{\rm jet}$	2.0	2.0	2.0	2.0
Ambient density	$\rho_{\rm amb}$	1	1	$1.1\ 10^{-3}$ g cm^{-3}	$2.34\ 10^{-26}$ g cm^{-3}
Sound speed	$c_{\rm amb}$	1	1	$3.4\ 10^{4}$ cm s^{-1}	$6.72\ 10^{7}$ cm s^{-1}
Ambient parameters:					
Ambient temperature	$T_{\rm amb}$	n/a	n/a	300 K	$2.0\ 10^{7}$ K
Internal energy	$u_{\rm amb}$	0.9	0.9	$2.53\ 10^{6}$ erg cm^{-3}	$9.53\ 10^{-11}$ erg cm^{-3}
Ambient pressure	$p_{\rm amb}$	0.6	0.6	$1.01\ 10^{6}$ dyn cm^{-2}	$6.35\ 10^{-11}$ dyn cm^{-2}
Pressure ratio	$p_{\rm jet}/p_{\rm amb}$	2.0	2.0	2.0	2.0
Density ratio	$\rho_{\rm jet}/\rho_{\rm amb}$	0.1	10	0.1	0.1
Jet speed	$v_{\rm jet}$	8.94	0.89	$2.48\ 10^{5}$ cm s^{-1}	$4.03\ 10^{9}$ cm s^{-1}
Mass flux	$\dot{\mathcal{M}}_{\rm jet}$	2.81	28.1	$24.9\ 10^{3}$ g s^{-1}	2.80 M$_\odot$ yr^{-1}
Thrust	$P_{\rm ram}$	25.1	25.1	$6.40\ 10^{9}$ dyn	$7.12\ 10^{35}$ dyn
Kinetic power	$L_{\rm jet}$	112.4	11.2	$8.23\ 10^{14}$ erg s^{-1}	$1.51\ 10^{45}$ erg s^{-1}
Nozzle time-scale	$t_o = r_{\rm jet}/c_{\rm amb}$	1	1	$0.4\ \ 10^{-3}$ s	3.64 Myr
Dynamical time	$D/v_{\rm jet}$	3.35	33.5	$1.57\ \ 10^{-3}$ s	1.82 Myr
Simulated time	$t_{\rm stop}$	200	200	$32\ \ 10^{-3}$ s	728 Myr

Notes. Note that the astrophysical jets generally require further physics to be consistent. These will be added once the fundamental behaviour is rigorously established. The parameter $n_{\rm p,\ amb}$ is the hydrogen nuclei (free proton) density in the ambient medium.

Note that the PLUTO code also contains recipes for relativistic fluid dynamics, cooling, and magnetohydrodynamics, as well as numerous other algorithms developed by the user community (e.g. Ahmane et al. 2020; Barkov & Bosch-Ramon 2022). However, in this paper, we restrict our analysis to that of non-relativistic hydrodynamics.

2.2 The scaling

The jet radius is set to $R_{\rm jet} = 1$. By setting the initial ambient sound speed also to 1, $c_{\rm amb} = 1$, the unit of time is $R_{\rm jet}/c_{\rm amb} = 1$. We complete the set up by putting the initial ambient density $\rho_{\rm amb} = 1$.

Given an ambient density of one unit and

$$c_{\rm amb} = \sqrt{\frac{\gamma \times p_{\rm amb}}{\rho_{\rm amb}}}, \tag{1}$$

yields a pressure $p_{\rm amb} = 1/\gamma = 0.6$ and internal energy per unit volume $u_{\rm amb} = p_{\rm amb}/(\gamma - 1) = 0.9$ for the specific heat ratio of $\gamma = 5/3$, since

$$p_{\rm amb} = (\gamma - 1)u_{\rm amb}. \tag{2}$$

We will also employ a ratio of specific heats at constant volume, $C_{\rm V}$.

Three parameters are specified to describe the jet at the nozzle: the Mach number, M, the pressure ratio $\kappa = p_{\rm jet}/p_{\rm amb}$, the density ratio $\eta = \rho_{\rm jet}/\rho_{\rm amb}$. We fix the jet Mach number, M, and then determine the jet speed as $v_{\rm jet} = Mc_{\rm jet}$, where $c_{\rm jet}^2 = \kappa/\eta$. The values for the specific illustrated examples are provided in Table 2.

We assume adiabatic media so that all quantities can be scaled. We may thus consider whether our simulations represent both a supersonic rocket exhaust or a radio galaxy as far as scale is concerned. For the example parameters detailed in Table 1, the scale size and dynamical time-scales run between centimetre and megaparsec, and milliseconds to 100 Myr, respectively.

The main sets of simulations were performed on uniform cylindrical grids of 200 radially distributed zones and $200 \times M$ along the axis. This converts into lengths of $15R_{\rm jet}$ and $15M\ R_{\rm jet}$, respectively. Hence, the axial length of the grid is proportional to the Mach number, anticipating that the flow pattern will be stretched to some extent.

Table 2. Summary of parameters and figure numbers for the illustrated simulations.

Pressure ratio, κ	Density ratio, η	Derived jet speed	Resolution zones/$R_{\rm jet}$	Figure
2	0.1	8.944	13.33	2/3
2	0.1	8.944	53.33	4/5
4	0.1	12.65	13.33	6
16	0.1	25.30	13.33	7/8
2	10	0.894	13.33	9(a) /10(a)
2	10	2.530	13.33	9(b) /10(b)
1.2	0.1	6.928	13.33	11

We aim to maintain a free environment that is sufficiently large so that disturbances are not trapped close to the jet. In addition to a limit on the change to the time-step on entry, we take the following two steps.

First, we extend the computational domain by $50R_{\rm jet}$ and $100\ R_{\rm jet}$ in the radial and axial directions, respectively. This is done by adding 100 and 200 zones on standard format staggered grids on to the uniform section. Reflection boundary conditions are applied to the axis and the plane containing the orifice.

Secondly, we ramp up the jet speed linearly from an initial value of zero up to the constant $v_{\rm jet}$. We take a default time to reach the final speed as $t_{\rm ramp} = 10$ after trying numerous values and finding no significant difference to the flow pattern once beyond 100 time units. Hence, over the long time-scale, the ambient pressure recovers from the effect of the initial advancing bow shock.

Five properties are recorded to file at each of 1000 dumps separated by 0.2 time units, allowing evolution over 200 time units. The parameters are the density, ρ, pressure, p, two velocity components, v_z and v_r, and a mass-weighted jet tracer, χ. Hence, the possibility to include a non-zero azimuthal velocity is not considered.

In Appendix A, we present the fundamental formula for the mass flux, momentum flux, and power through any cross-section. The momentum flux is written in terms of the ram and thermal pressure.

The power is expressed in terms of the combination of enthalpy and kinetic energy.

3 OVERPRESSURED FLOW TYPES

The propagation of waves into the jet from the nozzle lip will occur at the Mach angle. Therefore, there is an undisturbed conical zone with a cone half-angle of $\sin^{-1} 1/M$. This is followed by a so-called silent zone in which the jet is in free expansion. At very low overpressures, sound waves propagate into and out of the jet, with a wavelength of $\sim MR_{\rm jet}$ (Sanders 1983).

We will here establish the existence of three types of flow pattern in the κ–M phase space.

At low overpressures, a significant expansion fan emanates from the nozzle lip. The result is that the jet over expands since the free expansion in the silent zone has reduced the axial pressure. Hence, compression waves recollimate the flow. These waves lead to an oblique shock pattern that repeats downstream, forming a diamond chock pattern referred to as regular reflection. As we will show, the apex of the conical shock crosses the jet axis at a stand-off distance related to the Mach number and some power of the pressure ratio:

$$D_1 = \sqrt{(M^2 - 1)}\kappa^{\beta} R_{\rm jet}. \quad (3)$$

Here, at very low overpressures, the minimum distance, $d_{\rm M}$, should be just beyond that given by the Mach angle, D_0: $d/R_{\rm jet} \geq D_0/R_{\rm jet} = \arcsin 1/M$. The simulations below determine $\beta \sim 1.2$ for the particular range of conditions chosen here.

At high overpressures, the shock pattern appears as shown in Fig. 1. The diamond pattern is replaced by a Mach shock disc across the jet, which connects the oblique shocks together at what is termed a triple point (i.e. a triple circle in cylindrical symmetry). This pattern is termed Mach reflection.

This transformation is caused by the free jet expansion along the jet axis that has reduced the thermal pressure to a very small value. Hence, the Mach disc location is determined by the balance between the ram pressure in the free expansion and the ambient pressure. Early experiments found the dependence on pressure and Mach number was consistent with this explanation. While clearly a matter of detailed two-dimensional integration, a simple analytic formula calibrated to experiments, yields (Carlson & Lewis 1964)

$$D_1 = 1.38\gamma^{1/2}\kappa^{1/2} M R_{\rm jet}. \quad (4)$$

This formula was also found to be applicable when the ambient medium flows over the nozzle by Buckley (1975), where a summary of the early experiments can be found.

The most recent comprehensive review by Franquet et al. (2015) upholds the above result. They remark that the Mach shock disc location is the only reliable quantitative measure of a flow and collate a wealth of data up to a Mach number of 3. They also note the effects due to instabilities, hysteresis, and apparatus configuration.

In addition, we can consider the intermediate pressure regime to have a distinct character in which further oblique shocks follow the initial stand-off Mach disc. This creates a complex series of oblique shocks. These regimes are most prominently separated for the Mach 2 case that we analyse in this paper.

4 RESULTS: MACH NUMBER OF 2

4.1 Analysis tools

The first of two basic analysis tools are the four-panelled diagrams displaying distributions of four of the physical parameters in the z–r plane of the cylindrical coordinates. Fig. 2 shows the density, axial velocity, jet tracer, and pressure for the $M = 2$ and $\kappa = 2$ simulation. The jet tracer is mass weighted with a value of one for the material originating from the jet and zero for the ambient gas.

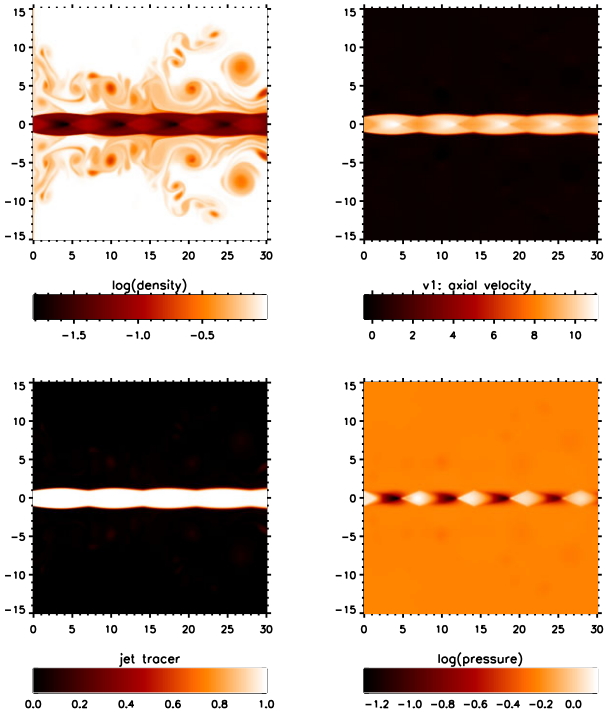

Figure 2. The distributions of physical parameters for a Mach 2 jet with overpressure $\kappa = 2$ and density ratio $\eta = 0.1$. The time $t = 200$ corresponds to the end of the run. The length-scale is in units of the jet radius. Upper left-hand panel: density, upper right-hand panel: axial velocity component, lower left-hand panel: tracer for jet gas, lower right-hand panel: pressure.

Note that shock fronts are particularly prominent in the pressure panel where sharp gradients are found. On the other hand, the density panel emphasizes the long-lived vortices created in the ambient gas by the shearing motion.

Also note that the entrance sound speed of the jet is $\sqrt{20}$ for these parameters. This yields a jet speed of 8.944. The speed downstream then alternates regularly between approximately 8 and 11 units.

The second analysis tool is a space–time diagram that shows the evolutionary nature by displaying the pressure profile along the jet axis for each of the 1000 time dumps each separated vertically by a time of 0.2. In Fig. 3, one notices the propagation of the initial bow shock into the uniform medium to the lower right. After the initial impact phase, the flow pattern converges to a largely steady state with short-term oscillations superimposed.

The speed at which the jet head crosses the grid is measured to be 1.22. This is consistent with the flow pattern as discussed in Appendix A. This is also the speed at which the small pressure disturbances propagate in a criss-cross pattern within the jet until a steady flow pattern is approached after about 150 time-steps.

4.2 Resolution

Besides the standard resolution of the above figures, we have performed doubled and quadruple resolution simulations, taking $M = 2$ and $\kappa = 2$ for illustration. Fig. 4 displays the physical parameters for a uniform grid of 800 × 1600 at the time of 200.

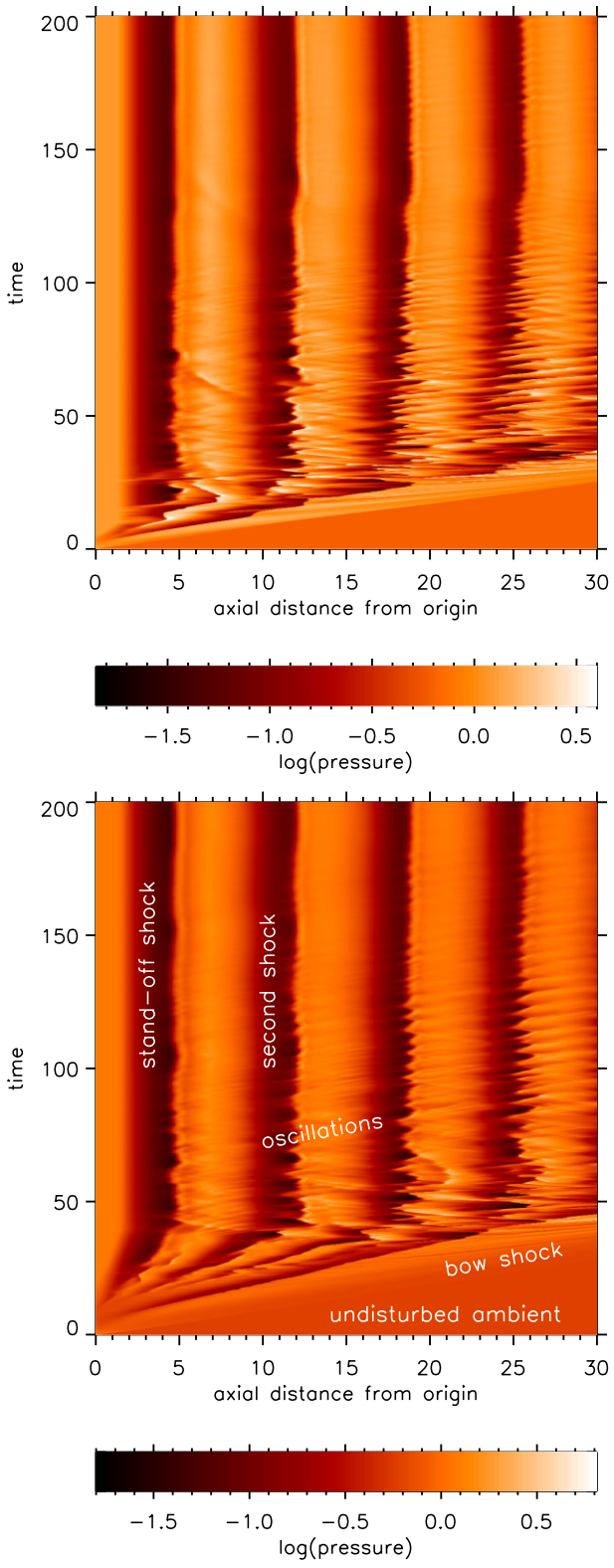

Figure 3. The distribution of the pressure along the jet axis as a function of the time for a Mach 2 jet with overpressure $\kappa = 2$ and density ratio $\eta = 0.1$. The length-scale is in units of the jet radius. The two panels differ only in the imposed initial ramp of jet speed up to the final values. Top diagram: The jet speed increases linearly over the first 10 time units. Lower panel: The jet speed increases linearly over the first 40 time units.

The density in the top left-hand panel of Fig. 4 emphasizes the that the vortices in the ambient medium are now more numerous and smaller. The contrast in terns of density remains similar to the low-resolution run: A vortex eye originates as partly jet gas and is of low density.

In the jet, the high resolution is able to resolve the converging of gas on to the axis. A small Mach disc appears, which reduces the speed in a channel close to the jet axis as seen in the top right-hand panel.

For the evolution, Fig. 5 shows a sharper resolution of the pressure oscillations. While better defined, the fingers are not of greater amplitude or frequency than in the low-resolution run.

The first stand-off shock shows smeared out oscillations at low resolution even at the end of the run. These can be seen distinctly at high resolution, although still of low amplitude in size and pressure.

Most striking is the strength of the intermediate shocks that are unique to these intermediate overpressures. These will develop into full Mach discs at higher overpressures, while the inner shocks, which obey the linear relationship, become weak.

4.3 The high overpressure regime

While the repeated diamond pattern dominates for overpressures below 2.5, a transformation to a Mach shock disc occurs between 2.5 and 4. As shown in Fig 6, the Mach shock disc has completely disrupted the regular reflection pattern. The jet pressure falls steeply from the nozzle and never recovers to the high values. However, at this stage, there is still a recollimation zone as seen in the lower left-hand tracer panel. A low-density and high-negative velocity is present along parts of the jet axis.

A defining feature of these transition states is the high speed sheath that surrounds the jet core. Such a sheath was found in previous simulations and proposed as a model for volcanic gas eruptions from vents (Ogden et al. 2008).

At extreme overpressures, the Mach disc cuts almost the entire jet, as shown for $\kappa = 16$ in Fig 7. There remains a narrow high-speed sheath within which is a turbulent velocity structure albeit in axisymmetric mode. Note the extreme jet speed and low pressure reached just before the chock.

The evolution of the high κ flow is displayed in the space–time diagram off Fig. 8. Remarkable oscillations in the location of the shock are seen. The period of the oscillations remains approximately the same as for low overpressures.

However, there is now considerable mixing of the media in the downstream region, which leads to pressure disturbances propagating into and raising the pressure of the ambient medium. This, in turn, alters the effective overpressure from the initially imposed value. The consequence is that the location of the stand-off shock begins a long-term evolution that has a dramatic effect at higher Mach numbers (Keogh & Smith, in preparation).

5 DEPENDENCE ON DENSITY

The classical steady flow pattern of a jet depends only on the pressure and Mach number. We then do not expect any density dependence. However, the flow pattern is, in general, not steady and the density then comes into play with the inertia of a high-density jet likely to lead to greater stability.

The final snapshots of the two extremes in overpressure and flow pattern are shown in Fig. 9 for the jet-ambient density ratio of 10. Similar flow patterns to the low-density cases appear to be established.

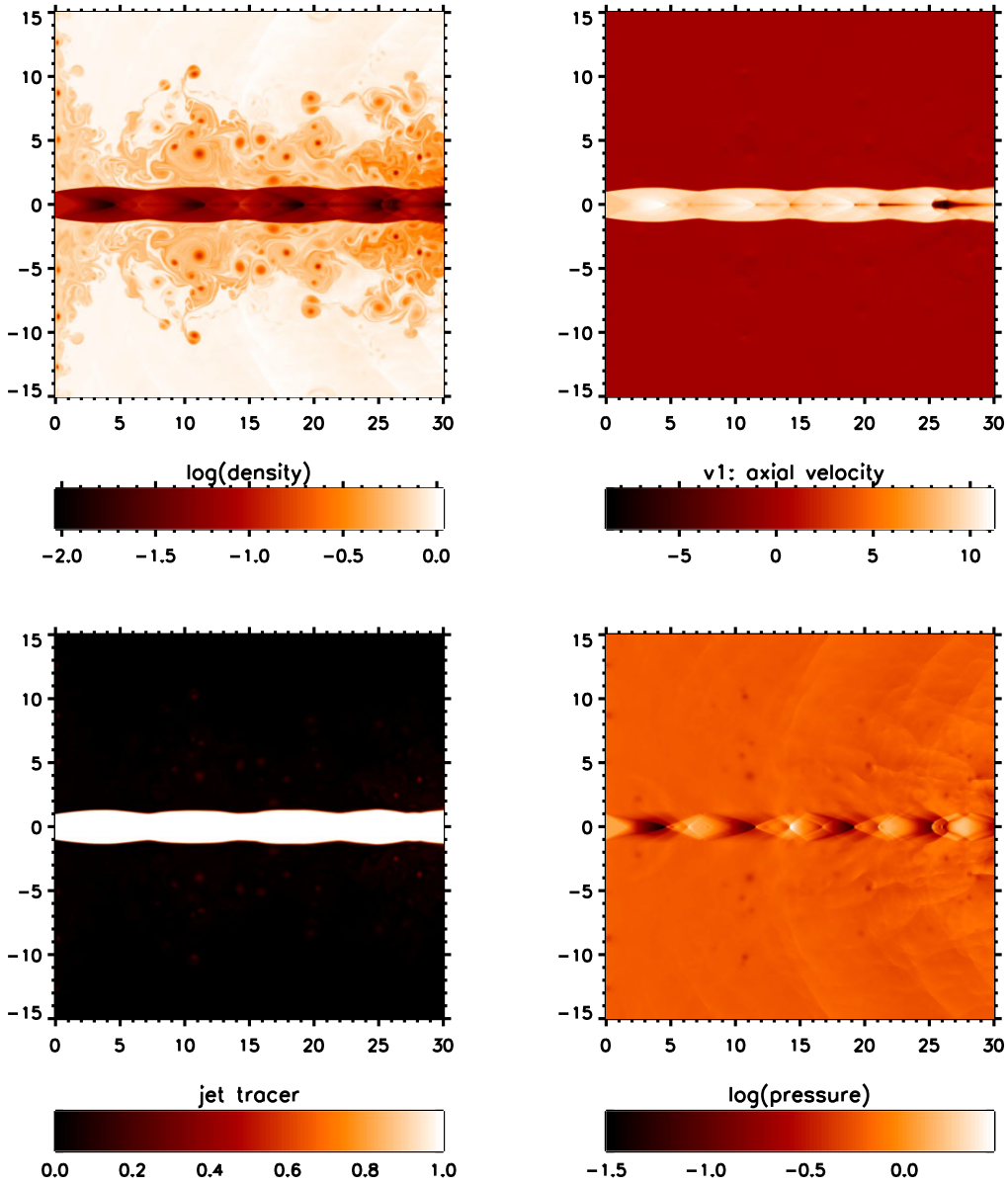

Figure 4. At the high resolution of 1600^2, distributions of physical parameters for a Mach 2 jet with overpressure $\kappa = 2$ and density ratio $\eta = 0.1$. The time $t = 200$ corresponds to the end of the run. The length-scale is in units of the jet radius. Upper left-hand panel: density, upper right-hand panel: axial velocity component, lower left-hand panel: tracer for jet gas, lower right-hand panel: pressure.

However, the oscillation pattern at the higher density contrasts to the lower density case. As displayed in Fig. 10, the oscillations remain with roughly the same amplitude but the time-scale is much longer and the propagation speed of waves is slower.

The oscillations seen in the shock location stem from pressure waves that run obliquely on the space–time diagrams. These oscillations generate waves in the ambient medium and are responsible for the high-pitched jet screeching, as sound waves propagate away from the jet (Powell 1953).

The frequency is density- and pressure-dependent. From the displayed simulations this is for $\kappa = 2$ roughly $0.6c_{\rm amb}/R_{\rm jet}$ for $\eta = 0.1$ and $0.24c_{\rm amb}/R_{\rm jet}$ for $\eta = 10$. For $\kappa = 16$, we estimate frequencies of $0.4c_{\rm amb}/R_{\rm jet}$ for $\eta = 0.1$ and $0.12c_{\rm amb}/R_{\rm jet}$ for $\eta = 10$.

Given the distances from the nozzle of the order of $10R_{\rm jet}$, these oscillations cannot be attributed to an entire feedback loop. Rather, a type of harmonic oscillation can be expected here as an expanding configuration will compress the adjacent ambient gas, raising the pressure temporarily. This pressure rise acts to reduce the overpressure felt by the jet, causing the stand-off distance and shock configuration to contract. The cycle is then complete as the contraction reduces the ambient pressure. The adjustment is then limited by the response time of the jet. Since the low-density jet begins with a sound speed 10 times higher than the high-density case (for a fixed overpressure), the pitch is expected to be 10 times higher.

As opposed to the regular oscillations that lead to high-frequency screeching, at high overpressures, this takes the form of noise as the entire flow loses coherency (Tam 1995). A third category of behaviour was not uncovered at these low Mach numbers. That is the catastrophic collapse of the flow due to an overwhelming pressure increase in the surroundings. This occurs in an unpredictable fashion only at high Mach numbers (in preparation).

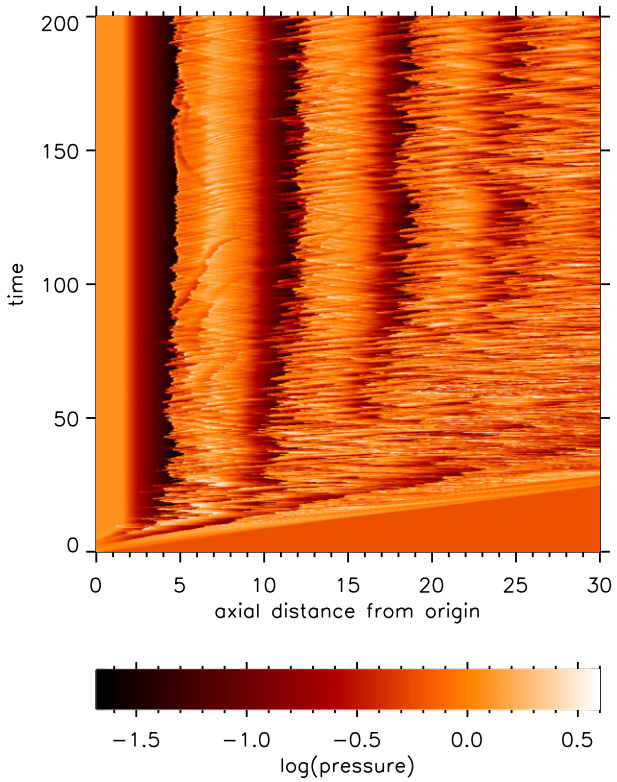

Figure 5. At a high resolution, the distributions of the overpressure along the jet axis as a function of the time for a Mach 2 jet with overpressure $\kappa = 2$ and density ratio $\eta = 0.1$. The length-scale is in units of the jet radius.

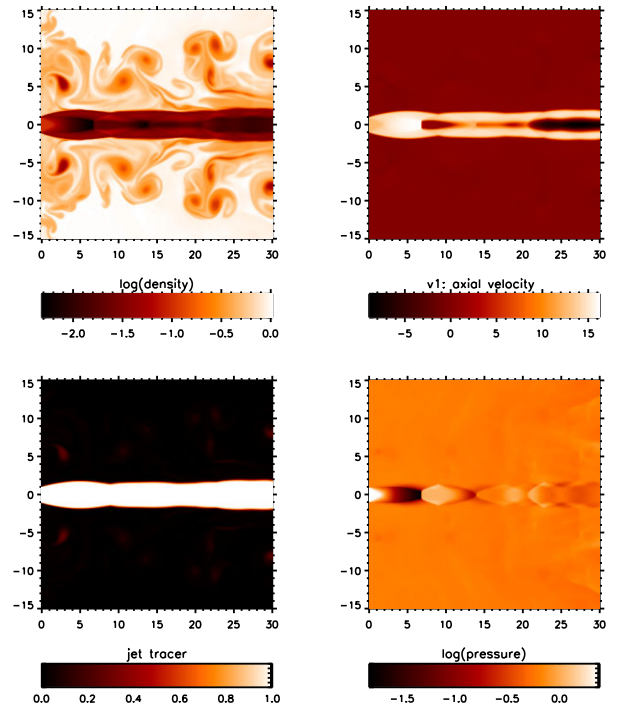

Figure 6. The distributions of physical parameters for a Mach 2 jet with overpressure $\kappa = 4$ and density ratio $\eta = 0.1$. The time $t = 200$ corresponds to the end of the run. The length-scale is in units of the jet radius. Upper left-hand panel: density, upper right-hand panel: axial velocity component, lower left-hand panel: tracer for jet gas, lower right-hand panel: pressure.

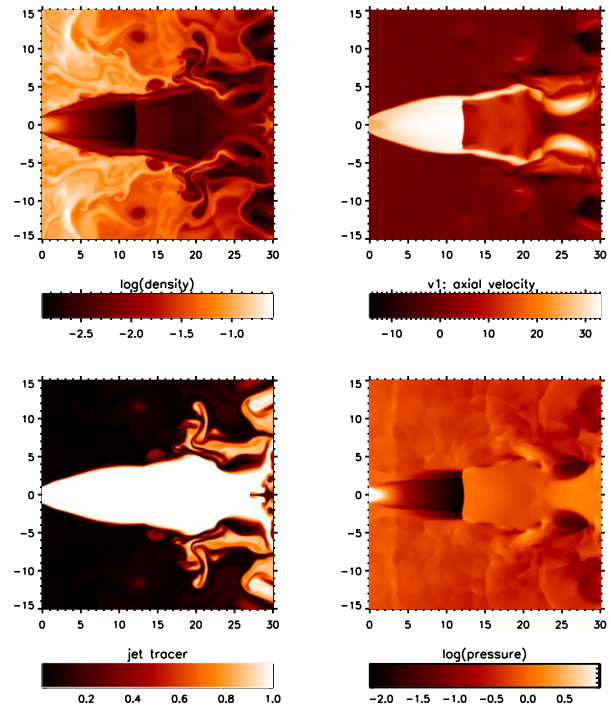

Figure 7. Mid-plane snapshots for $\kappa = 16$ and $\eta = 2$. The distributions of physical parameters for a Mach 2 jet with overpressure $\kappa = 16$ and density ratio $\eta = 0.1$. The time $t = 200$ corresponds to the end of the run. The length-scale is in units of the jet radius. Upper left-hand panel: density, upper right-hand panel: axial velocity component, lower left-hand panel: tracer for jet gas, lower right-hand panel: pressure.

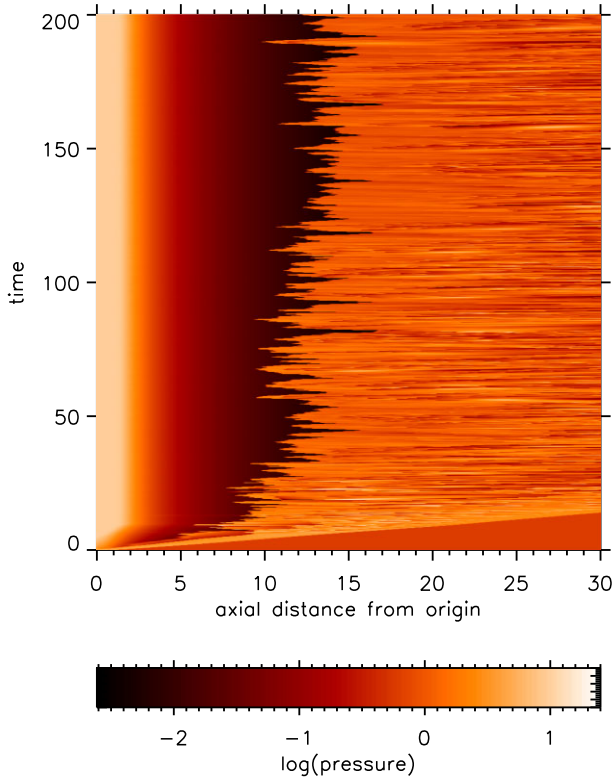

Figure 8. The distribution of the pressure along the jet axis as a function of the time for a Mach 2 jet with overpressure $\kappa = 16$ and density ratio $\eta = 0.1$. The length-scale is in units of the jet radius.

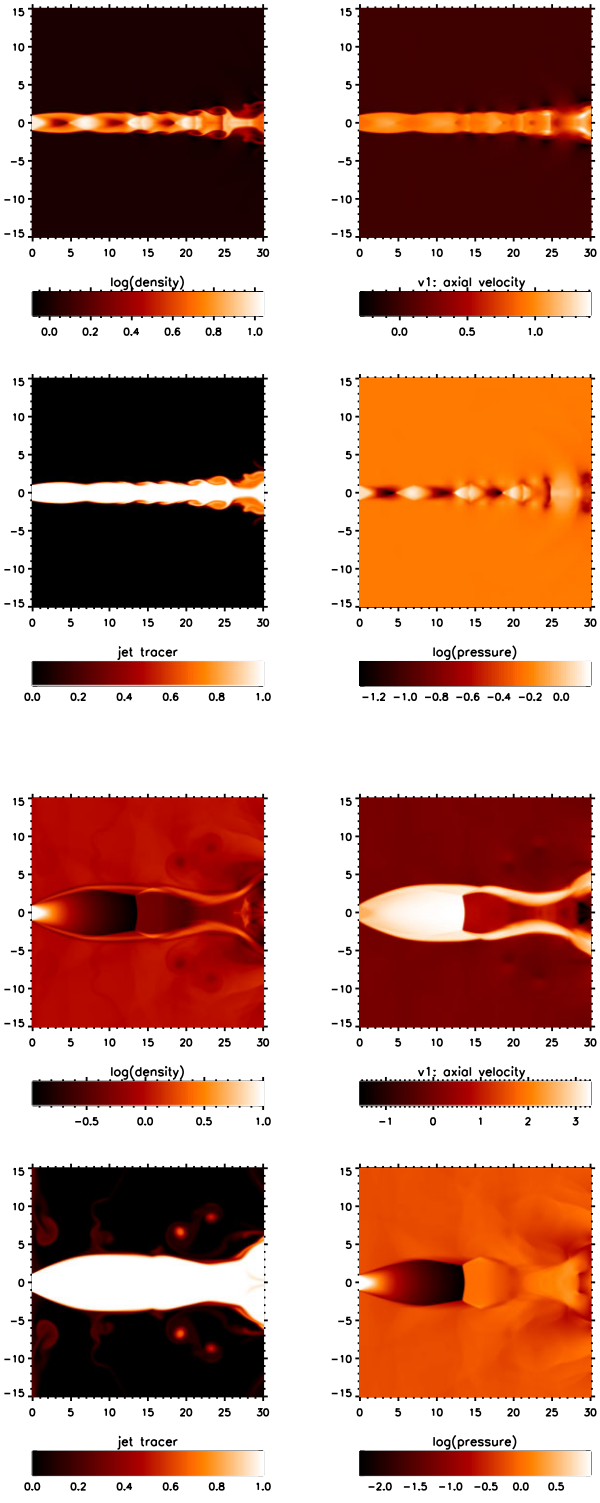

Figure 9. High-density ratio final snapshots. The distributions of physical parameters for a Mach 2 jet with overpressure $\kappa = 2$ (upper panel) and 16 (lower panel) and density ratio $\eta = 10$. The time $t = 200$ corresponds to the end of the run. The length-scale is in units of the jet radius. Upper left-hand panel: density, upper right-hand panel: axial velocity component, lower left-hand panel: tracer for jet gas, lower right-hand panel: pressure.

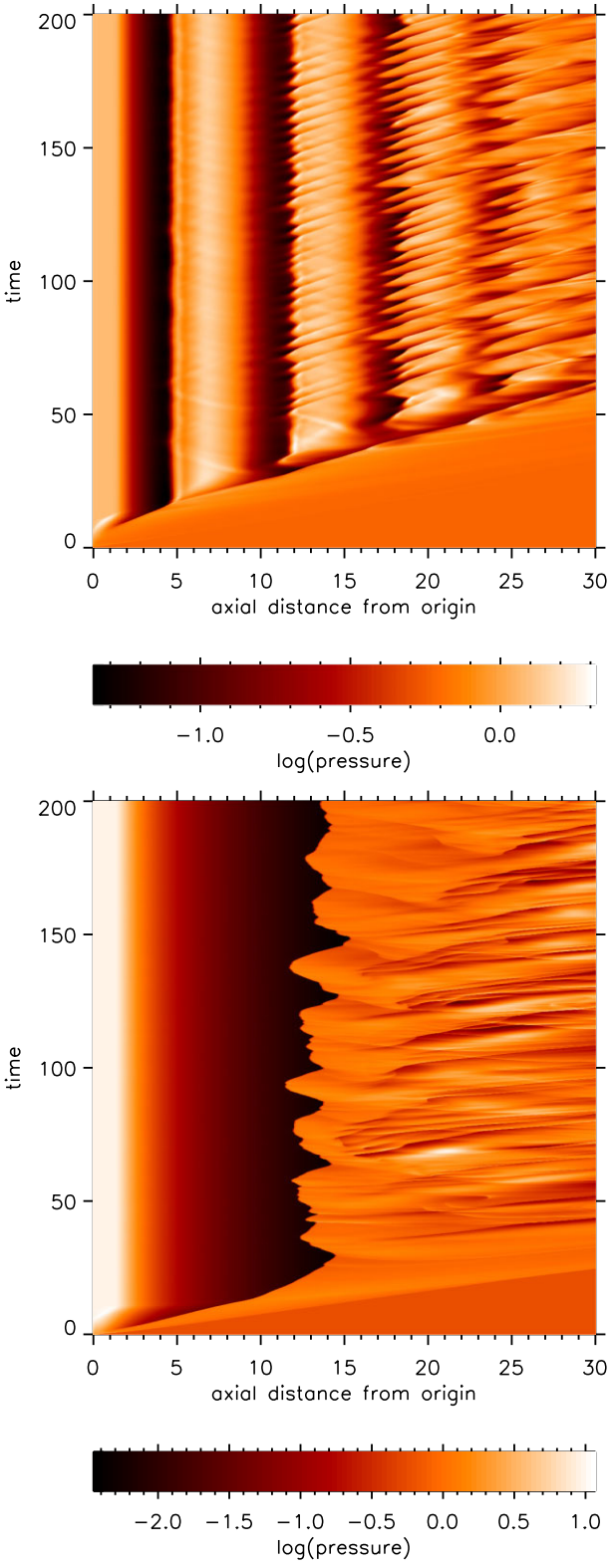

Figure 10. Space–time diagrams for a density ratio $\eta = 10$, a Mach 2 jet with overpressure $\kappa = 2$ (upper panel) and 16 (lower panel). The time $t = 200$ corresponds to the end of the run. The length-scale is in units of the jet radius.

The speed at which the jet interface traverses the grid is much slower at the high density. The speed is measured from the space–time diagrams to be ∼0.5 for $\kappa = 2$ and 1.0 for $\kappa = 16$. These values are somewhat smaller than those from equation (A9) due to the overall jet expansion and spread of the momentum over a larger area. For the low-density cases, we should expect crossing times of three times shorter. This is not recovered in the space–time plots above. This is due to the lower efficiency of propagation since the expansion of shocked gas inflated a cocoon.

Note that after this initial crossing, there are subsequent numerous pressure waves that traverse the diagrams at an oblique angle. The speeds are related to a balance of the momentum, a diagnostic for Kelvin–Helmholtz fluid instabilities. In the surface mode, we expect disturbances to propagate at the speed along a plane surface (Blake 1972) as well as a pinched cylindrical jet (Hardee 1979):

$$V_{\rm KH} = v_{\rm jet}\frac{\eta}{1+\eta}. \tag{5}$$

This implies that these waves cross the grid on a time-scale of ∼30 for $\eta = 0.1$ with the relatively high jet speeds. For the high-density, low-speed Mach 2 jets, the time-scale is ∼40. However, it is clear that at high overpressures, the flow is complex and numerical analyses are necessary.

At very low overpressures, the instability is apparent as it steadily grows along the jet, finally generating Mach shock discs as displayed in Fig 11. The dominance of the instability contrasts with the very steady $\kappa = 2$ simulation where the dominant diamond shock pattern inhibits the effect of the instability. We show here the case $\kappa = 1.2$ in Fig. 11 where the top panels display the spatial growth of the shock pattern while the lower panel displays the evolution, emphasizing the advection of the non-linear waves across the grid at a speed consistent with that given by equation (5).

6 JET POWER

6.1 Interchange between energy carriers

A contemporary issue of concern is the loss of energy from the jet into the environment. For rocket exhausts, this relates to the noise level (Tran et al. 2018).

For stellar jets, the level of support could restrict further star formation (Knee & Sandell 2000; Dionatos & Güdel 2017), while for extragalactic jets, the transfer of energy may regulate galaxy formation (Dubois et al. 2010). In particular, it is possible that jets could provide the support to the intergalactic medium, cutting off gas infall and quenching star formation (Dubois et al. 2010; Fabian 2012; Ehlert et al. 2022).

In general, jets become increasingly turbulent downstream, eventually dispersing all their energy and mixing the gas into the environment. In three-dimensional simulations, this can be fully explored with appropriate dynamical conditions included. We found that the initially evolving adiabatic jets, in the first six time-steps, efficiently transfer the majority of the jet kinetic energy into the heating of the ambient medium (Donohoe & Smith 2016). This energy transfer is mediated by shock and sound waves as the jet impacts the environment (Bambic & Reynolds 2019). In the case of rockets, the noise level can be suppressed by pre-spraying water into the air to absorb the sound waves (Lubert 2017).

Here, we explore how the energy continues to be distributed after the initial crossing of the jet and after the dynamical effects caused by the impact have dissipated. Our original expectation was that there would be no significant transfer unless we introduced pulsations or

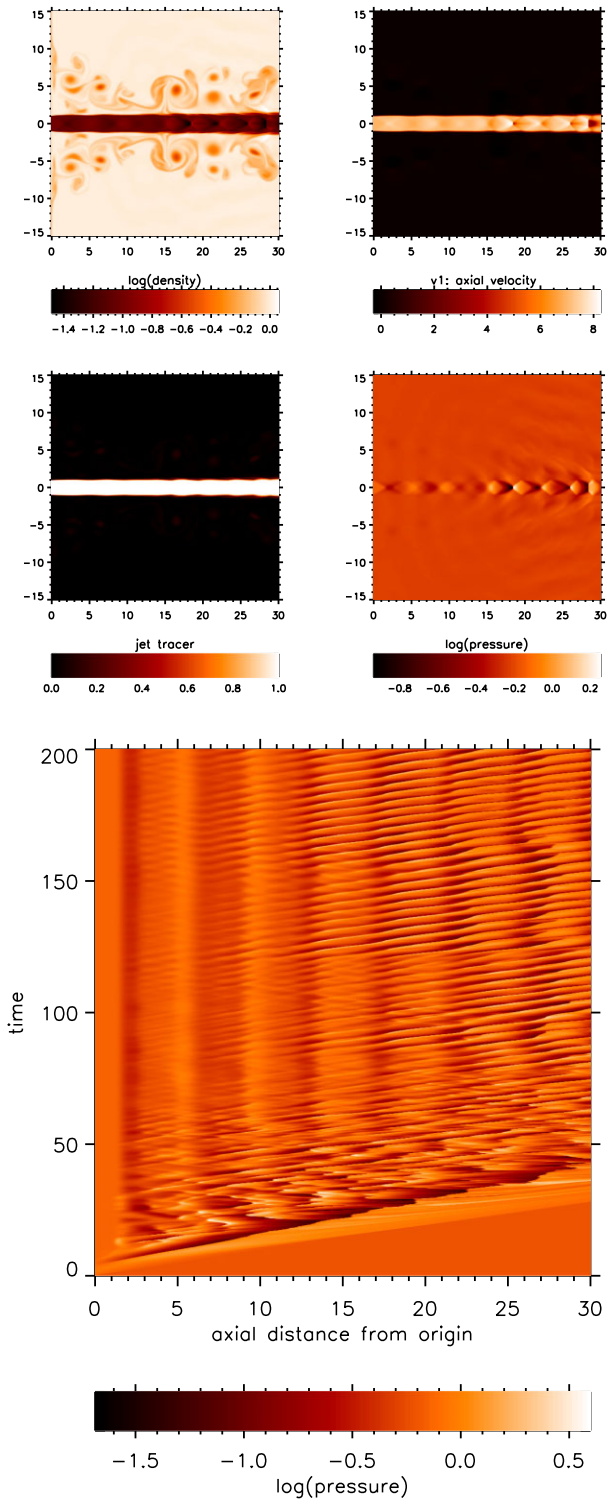

Figure 11. Low overpressure, $\kappa = 1.2$ example. The distributions of physical parameters and space–time diagram for a Mach 2 jet with overpressure $\kappa = 1.2$ and density ratio $\eta = 0.1$. The time $t = 200$ corresponds to the end of the run. The length-scale is in units of the jet radius. Upper left-hand panel: density, upper right-hand panel: axial velocity component, lower left-hand panel: tracer for jet gas, lower right-hand panel: pressure.

other variations to stop a steady flow pattern within a fixed channel from being set up. However, this proves not to be the case with the low-density jets being non-steady and transmitting a stream of sound waves into the surroundings. Hence, the energy is continually transferred into the ambient medium. The goal here is to determine the level of energy transfer. This will enable us to go on to study the contribution attributable to superimposed jet variations.

The rate at which each energy component flows along the grid is displayed in Fig. 12 for the three illustrative overpressures of $\kappa = 2$, 4, and 16 from upper to lower panels. The solid line in each panel indicates the power in the jet carried by the kinetic energy. Thus, at this low Mach number, the kinetic energy is seen to oscillate smoothly between the diverging and converging sections of the jet.

After the initial injection, energy is transferred from thermal into kinetic through the expansion. This is followed by a section within oblique shocks convert the kinetic back into thermal energy. Note that this cycle is very efficient with the kinetic energy reaching a minimum downstream of the stand-off distance along the axis. In fact, most of the power of the jet is conveyed through the outer sections of the jet away from the axis.

The total kinetic power carried across the grid in both media is provided by the dashed line. This shows that there is a narrow sheath corresponding to a boundary layer within which the two gasses merge and the numerical scheme operates to limit the viscosity into a narrow band.

In an adiabatic flow, no energy is lost through cooling or radiation. Energy can only be lost by mass flowing off the edges of the grid. This loss is minimal in our simulations since we have been careful to minimize the build-up of pressure gradients at the boundaries through the extended staggered grids. However, the total energy must include the work done through $p\mathrm{d}V$ to account for all the energy lost from the jet due to the high pressure.

The total power thus calculated is the flow of kinetic and enthalpy. This is shown in Fig. 12 as dotted and dot–dashed lines for the jet and combined media, respectively. Hence, it can be seen that the low-κ example flow has approximately reached a steady state within the jet. The combined power is slightly higher, corresponding to the advection of energy along the boundary sheath.

At high overpressures, as illustrated in the lower panel, the kinetic energy follows a very similar initial pattern dominated by the free expansion. The Mach shock disc then converts the kinetic into thermal through a strong shock. A coherent flow pattern is not regained and the flow is highly variable. One also notices the high total energy downstream, especially the peak in the ambient medium. This efficient transfer of energy into the ambient medium is balanced by the reduced power flows upstream and downstream. This is the completion of the feedback loop, which causes the location of the Mach shock disc to jitter, creating a turbulent flow downstream.

Remarkable behaviour is also present at the intermediate overpressure displayed in the middle panel of Fig. 12. Despite the insertion of the Mach shock disc, the flow remains quite steady, protected from the feedback loop by a thick sheath of fast forward-moving jet gas. There is no overall significant energy loss from the jet as indicated by the dotted line. Some motions remain in the ambient medium corresponding to the long-lived vortices visible in Fig. 6.

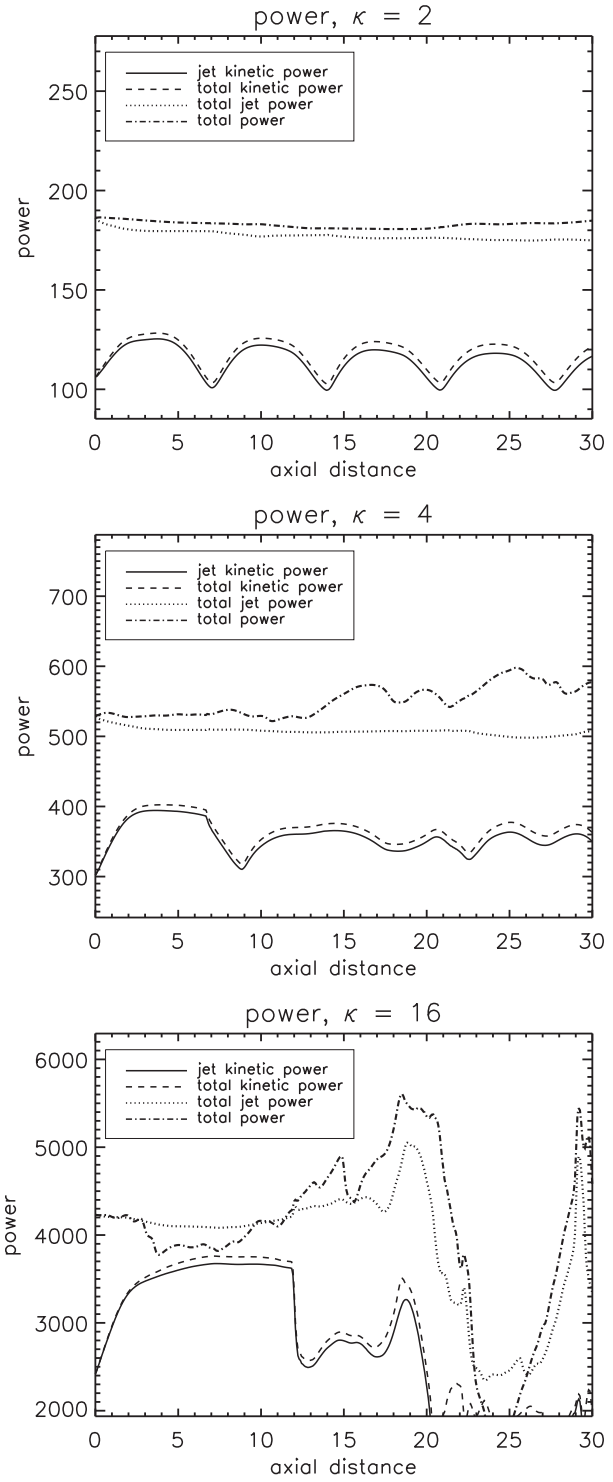

Figure 12. The integrated power over the entire circular cross-sections as a function of axial distance from the orifice boundary. A Mach 2 jet with density ratio $\eta = 0.1$ is taken, with overpressure $\kappa = 2$ (top panel), 4 (middle panel), and 16 (lower panel). The time $t = 200$ corresponds to the end of the run.

6.2 Lateral energy dispersion

In this subsection, we determine the fundamental means of energy transport. We are mainly concerned with the flux in the vicinity of the nozzle. Before this study, we suspected that there would not be any interchange with the environment because the jet rapidly

carves out a channel and then maintains this route. There is little dynamical interaction across the interface until Kelvin–Helmholtz waves become important. However, we have found that the turbulent plumes associated with Mach reflection, as well as the oscillations associated with regular reflection, are capable of driving a continuous flux of energy laterally into the surroundings.

Other dynamical effects will add to the energy dispersion on these small scales. Precession, short pulsations, and long episodes of jet activity will contribute, as evident on larger scales (e.g. Falceta-Gonçalves et al. 2010; Heinrich et al. 2021; Moya-Torregrosa et al. 2021). In particular, we found that the initial impact of the jet advancing on to the grid generates a large transfer of bulk kinetic jet energy into ambient thermal energy, found to be typically 70 per cent. That is not unexpected since the jet has to vacate a path for itself and the initial surrounding overspill into a cocoon. It should also be noted that other jet components including a magnetic field could result in different behaviour. However, a fundamental problem remains: how to transport energy into the environment far from the jet axis (e.g. Martizzi et al. 2019; Ehlert et al. 2021)?

We present here the effects of the Mach 2 overpressured jets on the distant environment by finding the energy flux through a large concentric cylinder of an axial length and radius of 360 and 180 zones on the 400–200 standard z–r domains. The net outflow across these locations is found as a function of time as shown for illustrative examples in Figs 13 and 14.

The first feature to note is the high lateral outflow during the first 40 time units, prominent in all panels (red/dotted lines) for the light jets in Fig. 13. This initial high peak corresponds to the jet blow-out of a cavity that expands work on the ambient medium. In the case of radio galaxies, the cavity appears as a depression in the soft X-ray emission (Smith & Donohoe 2021).

We previously found that about 70 per cent of the jet energy ends up as thermal energy of the ambient gas in this initial phase (Donohoe & Smith 2016). The leading bow shock acts to increase the pressure and internal energy but imparts a relatively small fraction of kinetic energy (green/dashed line). Hence, this is very similar to the previous studies of pressure-matched jets in which only the initial evolution was tracked.

The amount of energy that is laterally transmitted to large distances can now be calculated. We find that there is a very limited range of overpressures in which a net positive lateral flow of energy occurs. This is for light jets with overpressures between 1.4 and 2.5, as shown here in the middle panel of Fig. 13 This flow is driven by small regular oscillations in the jet flow that generate sound waves. However, the time-averaged amplitude of this flux does not reach more than ~ 3.5 per cent, once the flow has settled over the second half of the simulations.

Rather than a lateral outflow from the axis, a net inward flow of energy from the ambient medium occurs for high overpressures. The transition to a chaotic, turbulent pattern is complete by $\kappa = 6$, and is illustrated in the lower panel of Fig. 13. This indicates the tendency for a convection pattern to be established, in which the turbulent jet disturbs and drags ambient gas out with it. The ambient gas is replenished from the distant lateral reservoir, resulting in a negative energy balance.

A close inspection reveals a number of positive spikes in the lateral energy flux during the latter half of the simulation (red/dotted line). These spikes are interspersed with long periods of negative flux. Hence, disturbances reach far parts of the ambient medium but, overall, will provide little support.

In addition, for the light jets with low overpressures, the top panel demonstrates that there is a distinct pattern. Here, the jet energy flux

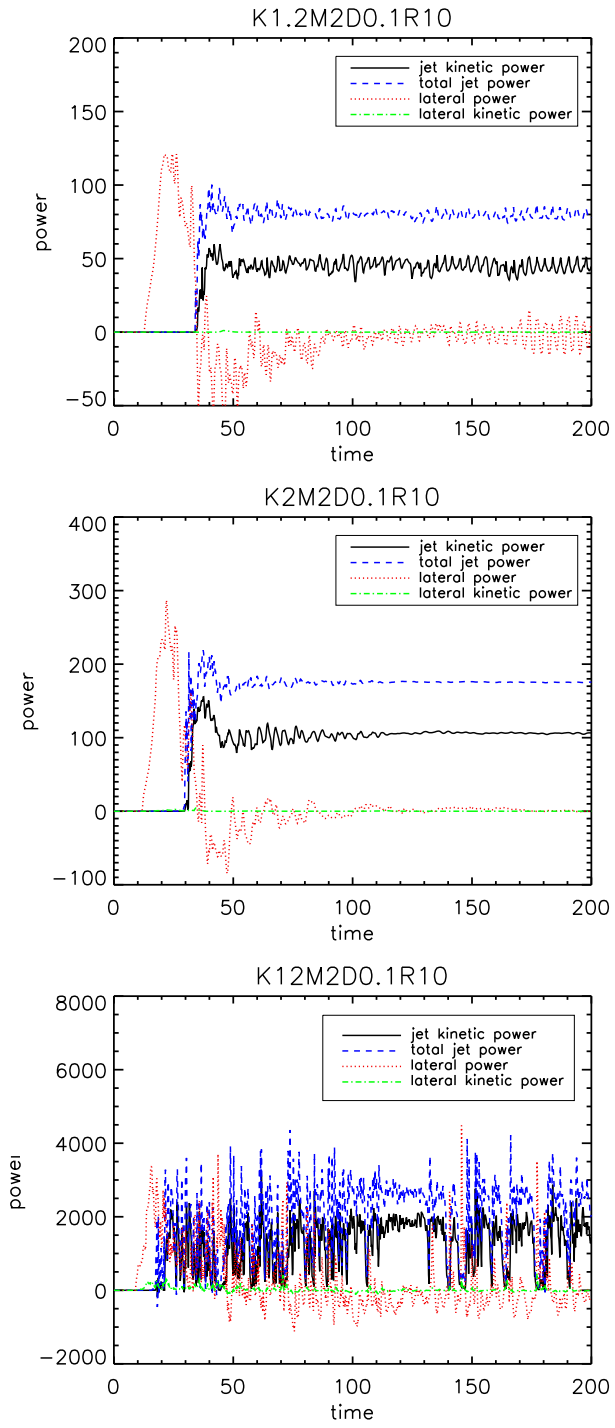

Figure 13. Evolution of the lateral and forward escape of energy for low-density jets. The energy flux is out of a cylindrical surface, drawn with a radius and axial length of 180 and 360 zones, respectively. Initially, the jet enters the grid and it takes ∼30 time units to cross to the cylinder cap, which is at 90 per cent of the uniform grid length. These are the net power outflows in simulation units. The panel titles correspond to the pressure ratio K, the relative jet density D, and the ramp time allocated to the initial linear increase in the jet velocity R.

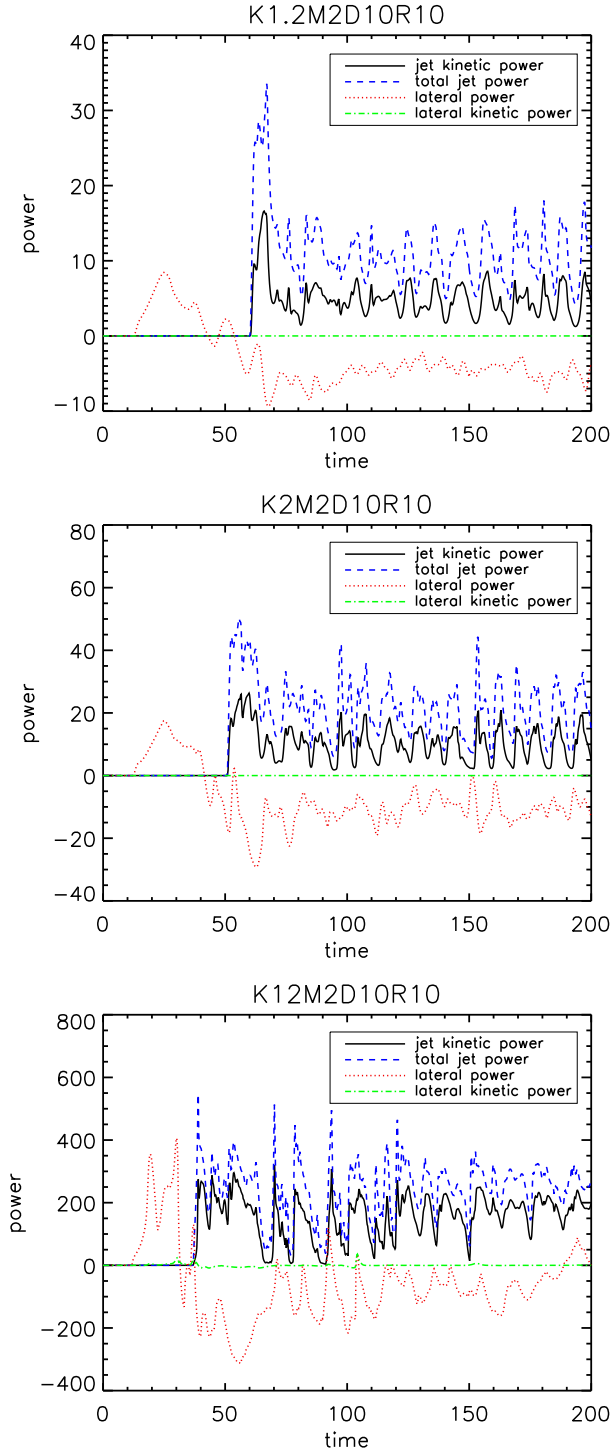

Figure 14. Evolution of the lateral and forward escape of energy for high-density jets. The energy flux is out of a cylindrical surface, drawn with a radius and length of 180 and 360 zones, respectively. Initially, the jet enters the grid and it takes ∼30 time units to cross to the cylinder cap, which is at 90 per cent of the uniform grid length. These are the net power outflows in simulation units. The titles ensure the panels are correctly included with K corresponding to the pressure ratio, D to the relative jet density, and R to the time allocated to the initial linear increase in the jet velocity.

displays regular oscillations and this is reflected in the net lateral flux that shows smooth oscillations about the zero flux line. This implies there is a sloshing of waves in the ambient gas that could have consequences in terms of the phases and stability of the gas. However, in the present steady jet simulations, the power associated would imply only a small feedback effect. Initially, the vortex-driven convection appears stronger when the jet is high density. As shown in Fig. 14, the inward flow of ambient gas is displayed in all cases through the negative values once the initial jet-driven bow has exited. The more massive but slower moving jet results in lower frequency oscillations that are still able to create a higher draught on to the surrounding gas. Hence, after the passage of the jet head, the heavy jet can then be more efficient in circulating the ambient medium. This is because jet powers are a factor of 10 lower for the heavy jets rather than stronger convection.

To summarize, lateral waves are found only for intermediate overpressures of the light jets. Little energy is transported in this manner. On the other hand, advective transport is capable of creating an energy flux through large vortex motions of the order of a few per cent for light jets and a few tens of percent for heavy jets, where steady flow patterns are not achieved. This could be related to the convection deduced from X-ray data (Kirkpatrick & McNamara 2015; Hillel & Soker 2017) that favour convection and mixing. On the other hand, many simulations yield high thermal energies and low kinetic/turbulent energy on the larges scales, suggesting that the convection in itself does not support an inward gas flow (Reynolds, Balbus & Schekochihin 2015; Weinberger et al. 2017).

7 THE STAND-OFF DISTANCE

The shock stand-off distance has been determined at the end point of each simulation. This is generally very easy to achieve since the pressure monotonically decreases along the axis until the first shock occurs. We find that we can apply a pressure increase of 1 per cent as an indicator of the cells where the shock front is located and then apply a local smoothing to more accurately fix the front position. For the very low overpressures, the 1 per cent condition might need to be reduced. We also tested with a higher pressure jump and a pressure jump proportional to κ. In both cases, the power-law indices are typically within 1–2 per cent different from those in Table 3.

The major issue with the shock location is that it is rarely stationary. We have therefore introduced a mean value and error to each data point by taking the average and the root-mean-square deviation over the final 10 recorded time-steps. These are the error bars presented in Fig. 15 and referred to in the least-squares analysis.

Fig. 15 displays the locations of the first three shock distances from the nozzle for the three densities indicated. These panels provide a visual measurement of the shock separations. We focused on the large-scale shock pattern and ignores sub-shocks. In this regard, once a shock was located, a further distance of at least 40 zones was required before searching for the subsequent shock.

The inner shock patterns, characterized by the diamond configurations, are very steady even out to the third shock. On the other hand, large error bars are associated with the Mach disc regime, especially for the low-density jets. This leads to a much stronger and monotonic increase in the stand-off distance with increasing κ for the high-density jets.

To quantify these findings, we present the corresponding log–log plots in Fig. 16. Superimposed are the power-law functions introduced in Section 3 that are excellent fits.

The dotted line corresponds to the formula 4, the form of which is guided and calibrated by experiment. This confirms the early studies

Table 3. Least squares fits to $\log\kappa - \log$ (shock distance) data in the linear form $y = A + Bx$ along with the sigma values generated by IDL programme LINFIT on using the root mean square values over the final five time units.

Density ratio	Shock number	κ range	y-intercept A	Gradient B	y-intercept error σ	Gradient error σ
$\eta = 0.1$	Stand-off	≤ 2.5	0.2607	1.2259	0.0004	0.0018
$\eta = 1$	Stand-off	≤ 2.5	0.2673	1.1973	0.0003	0.0017
$\eta = 10$	Stand-off	≤ 2.5	0.2673	1.1615	0.0002	0.0010
$\eta = 0.1$	Second shock	≤ 2.5	0.7817	0.9053	0.0007	0.0023
$\eta = 1$	Second shock	≤ 2.5	0.7831	0.8714	0.0012	0.0072
$\eta = 10$	Second shock	≤ 2.5	0.7838	0.8714	0.0009	0.0072
$\eta = 0.1$	Third shock	≤ 2.5	1.0601	0.6661	0.0015	0.0051
$\eta = 1$	Third shock	≤ 2.5	1.0597	0.6653	0.0043	0.0210
$\eta = 10$	Third shock	≤ 2.5	1.0610	0.6385	0.0027	0.0147
$\eta = 0.1$	Stand-off	> 2.5	0.6185	0.3903	0.0021	0.0044
$\eta = 1$	Stand-off	> 2.5	0.5286	0.5056	0.0028	0.0035
$\eta = 10$	Stand-off	> 2.5	0.5231	0.5078	1.1×10^{-6}	1.8×10^{-6}

and demonstrates that the stand-off distance is proportional to the square root of the initial overpressure in a wide range of conditions, even where we could expect the jet to have a profound effect on the ambient medium.

While the square-root regime is recovered at high κ, a linear regime is revealed here at low overpressures. This is indicated by the dashed line in Fig. 16. This shows that the numerical experiments yield a slightly higher power law.

Table 3 contains least-squares fit to the data. For this purpose, the data were divided into two ranges, with the low κ fit up to and including $\kappa = 2.5$. We thus conclude from this Table that the two regimes are well represented by linear and square root power laws. The provided σ errors to A and B indicate a few per cent uncertainty although the goodness of fit is actually low. Rather, high probabilities to power-law fits are only found when we superimpose errors of ~ 0, $1R_{\rm jet}$ to all data points, which can also be seen by inspection of Fig. 15.

In more detail, there is a systematic deviation from a linear law at low κ. Here, there is a fit of the form $y = 0.267 + 1.120x$, which translates to a power-law $D = 1.85\kappa^{1.20}$.

Given that signals propagate into the jet at the Mach angle of θ, where $\sin\theta = 1/M$, we could expect the axial pressure to begin to fall only beyond a distance $\sqrt{3} \sim 1.732$. Thus, the very weak shock front approaches very close to this point as $\kappa \rightarrow 1$.

The stand-off distance in the high-κ regime also deviates from the prediction of Section 3, which is $X = 3.56\kappa^{1/2}$ for the present conditions. The simulations yield a constant 10^A of 3.33–4.15. The square root behaviour is found except for the low-density case where a flatter power law is appropriate. This is in the sense that the Mach reflection is prone to collapse at high overpressures. The effect is caused by the influence on the ambient pressure when the stand-off Mach disc oscillates.

The axial position of the following two downstream shock fronts do not generally conform to power laws. As could be expected, after a Mach shock disc, the flow pattern is highly variable and shock fronts alter rapidly in position. However, at low overpressures, there is a good approximation to a linear increase, especially for the high-density jet.

Whereas for the first shock, the linear fit extrapolated back to a stand-off distance of 1.83 as $\kappa \rightarrow 1$, the second and third shock roughly approach additional distances of $2R_{\rm jet}M$, as would be expected, given a divergent-convergent wave pattern between fronts. To quantify this, we have found least-squares fits of the form $D_i = a + b\,\kappa$ for each front from which a simple subtraction for each separation. We thus find for the first shock

$$D_1 = \begin{cases} 1.81 + 2.43(\kappa - 1) & \eta = 0.1 \\ 1.82 + 2.41(\kappa - 1) & \eta = 1.0, \\ 1.82 + 2.41(\kappa - 1) & \eta = 10 \end{cases} \quad (6)$$

which are very close. The distance to the next shock is then easily expressed:

$$D_2 - D_1 = \begin{cases} 4.56 + 2.47(\kappa - 1) & \eta = 0.1 \\ 4.39 + 2.61(\kappa - 1) & \eta = 1.0. \\ 4.37 + 2.63(\kappa - 1) & \eta = 10 \end{cases} \quad (7)$$

The distance out to the third shock is

$$D_3 - D_2 = \begin{cases} 5.61 + 1.30(\kappa - 1) & \eta = 0.1 \\ 5.69 + 1.30(\kappa - 1) & \eta = 1.0. \\ 5.46 + 1.28(\kappa - 1) & \eta = 10 \end{cases} \quad (8)$$

These results clearly show that the shock separation gradually increases away from the minimum value we could expect of $2MR_{\rm jet} = 4$. This would at least partly be due to a gradual increase in the jet radius with each subsequent convergence.

8 DISCUSSION

8.1 The oscillations

We demonstrate below that the oscillation frequencies measured in the simulations are consistent with those expected from the propagation of surface waves. The frequency is determined by the rate at which the jet channel can expand and contract in response to variations in the jet overpressure.

These morphological changes are thus closely related to Kelvin–Helmholtz wave propagation between the nozzle and the stand-off shock. Previous work in this high-frequency screeching has proved inconclusive. The problem is non-linear and the feedback loop complex, as reviewed by Gao & Li (2010).

A relevant dynamical time-scale for the nozzle flow is given through the stand-off distance and the initial jet speed. For low κ, we use the formula for regular reflection (equation 3) to yield the value

$$t_{\rm d} = \frac{D_1}{v_{\rm jet}} = \sqrt{(1 - 1/M^2)}\kappa^{\beta - 1/2}\sqrt{\eta}, \quad (9)$$

in the usual units of $R_{\rm jet}/c_{\rm amb}$.

A second time-scale is the dynamical time for Kelvin–Helmholtz surface waves to traverse from the nozzle to the stand-off shock. This

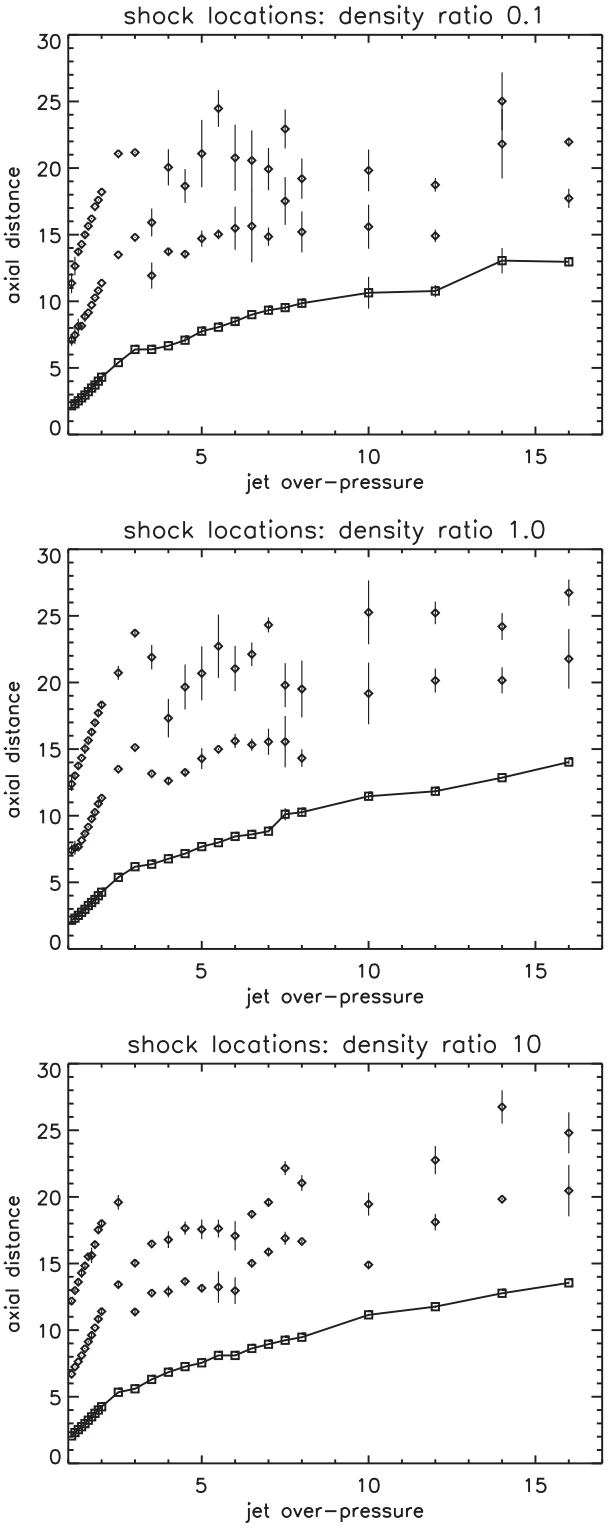

Figure 15. The shock front distances of the first three shocks along the jet axis as a function of the overpressure, κ, in units of the jet radius. Upper panel: Mach 2, density ratio $\eta = 0.1$. Lower panel: Mach 2, density ratio $\eta = 1$. The stand-off shock locations are designated with square symbols and the outer shocks with diamonds.

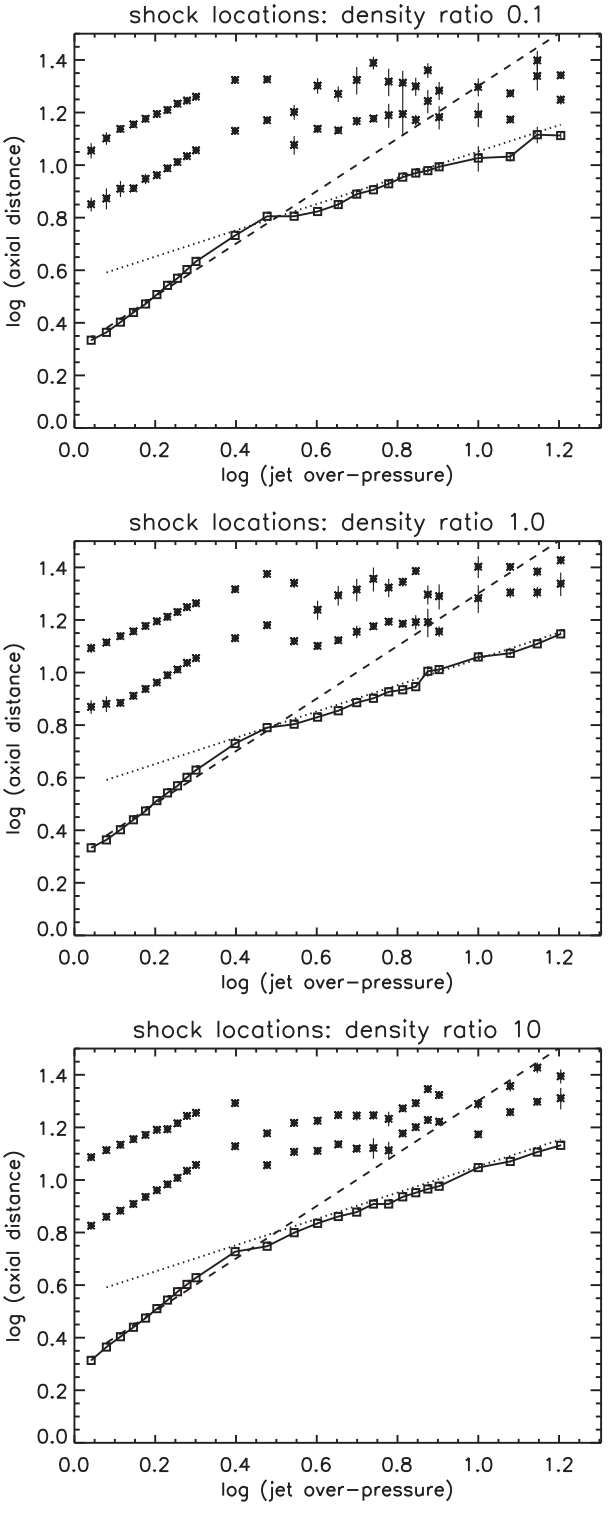

Figure 16. The logarithm of the shock distance of the first three shocks along the jet axis as a function of $\log \kappa$ in units of the jet radius. Upper panel: Mach 2, density ratio $\eta = 0.1$. Lower panel: Mach 2, density ratio $\eta = 1$. The analytic power laws superimposed are those from Section 3 with slopes 1 (dotted line) and 0.5 (dashed line).

is expected to be related to the ability of the morphology of the jet structure to change. From equation (A9), we find

$$t_{\rm KH} = \frac{D_1}{V} = \sqrt{(1 - 1/M^2)}\kappa^{\beta-1/2}(1 + \sqrt{\eta}). \quad (10)$$

This gives values of $t_{\rm KH} = 1.85$ for the low-density case and $t_{\rm KH} = 5.86$ for the high-density case for $\kappa = 2$, and $\beta = 1.2$. These predicted values compare quite well to the time periods found in Section 5 of 1.67 and 4.16, respectively, for the average oscillation time-scales.

For high κ, we use the formula for Mach shock discs, equation (4), to yield the value

$$t_{\rm d} = \frac{D_1}{v_{\rm jet}} = 1.38\sqrt{(\gamma\eta)}, \quad (11)$$

in the usual units of $R_{\rm jet}/c_{\rm amb}$. In this case, we find

$$t_{\rm KH} = \frac{D_1}{V} = 1.38\sqrt{\gamma}\ \ (1 + \sqrt{\eta}), \quad (12)$$

independent of the pressure. This takes values of $t_{\rm KH} = 2.3$ for the low-density case and $t_{\rm KH} = 7.4$ for the high-density case for $\kappa = 2$. Again, these predicted values compare well to the time periods found in Section 5 of 2.5 and 8.3, respectively.

We thus find that the computed fluctuation time-scale is proportional to the square root of the density ratio and that this is consistent with wave propagation at the surface wave convective speed. This is consistent with the acoustic analysis presented by Gao & Li (2010), who found that the convective wave speed depends on the inverse square root of the temperature ratio for low-pressure differences.

In summary, the good correspondence between the wave speeds and the oscillations strongly suggest that waves propagate through the channel with the ambient gas being pushed and pulled by the internal motion of the shock fronts at the relevant Kelvin–Helmholtz speed.

8.2 Feedback

A jet provides a route for feedback from a central engine to the disturbed part of the ambient medium (Martí 2019). The energy so transported and subsequently transmitted into the distant surroundings could hold up further infall and so turn off the supply of fuel. On the other hand, a jet may create supersonic turbulence that can enhance the infall at least temporarily (Fabian 2012).

A number of simulations have now shown that the initial jet impact and leading bow shock results in a power supply with 60–80 per cent of the energy going into thermal energy in the ambient medium (Hardcastle & Krause 2013; Donohoe & Smith 2016; Bourne & Sijacki 2021; Huško & Lacey 2022).

However, once the bow shock has cut a path through the ambient core, there would not be a significant continued supply of energy if the flow pattern becomes stationary. Prasad, Voit & O'Shea (2022) show that taking a narrow jet opening angle reduces the thrust per unit area and so increases the long-term coupling with the ambient gas. The simulations presented here allow us to quantify the amount of energy that may aid the support of the inner core. The oscillations in the flow pattern continue to couple the jet and ambient gas well after the jet has exited the core region. The coupling is at most a few per cent of the jet energy although the sporadic release of larger spikes have short-term effects. Hence, this is best described as noise with booms superimposed. Note that the opening angle in our simulations is set by the expansion of the parallel flow at the nozzle exit rather than an imposed conical opening.

It is clear that momentum transfer from the jet will tend to drive out the ambient gas that lies adjacent to the lobes. As applied to cluster cooling flows, both the circulation and infall can be induced (Yang & Reynolds 2016; Weinberger et al. 2017). Here we note more generally that the circulation pattern and outward transport of core material results in a flow towards the jet axis.

There is also evidence that the feedback loop leading to the oscillations in the flow pattern are enhanced by the inner wall that harbours the nozzle (as best visible in generated movies). This wall forces the pressure of inward moving waves to rise and be reflected. Follow-up simulations will be required to elucidate this as well as to study the effect of air flow external to the jet as would be experienced by rocket exhausts.

8.3 Radio galaxies

Direct application of these results requires an interface between the distributions of physical parameters presented here with both the emission mechanism and the radiative transfer processes. We achieved this for the pressure-matched jet simulations in Smith & Donohoe (2019). Those three-dimensional simulations sought to link the degree of precession of the jet axis to the degree of limb-darkening of a radio lobe. The simulations covered an equivalent time-scale of just six units. They demonstrated that if the jet has a varying direction then the so-called limb-darkened Fanaroff–Riley type I radio sources (Fanaroff & Riley 1974) can be created. In addition, the inclination angle between the jet axis and the observer, the dynamical range and the spatial resolution all comtribute to the classification based on just the two types.

A different type of duality between edge-darkened and edge-brightened structures is generated from low Mach number simulations. We could claim that the radio galaxy morphology is related to the dichotomy in the physical structures brought about by the overpressure. We have shown that turbulent plumes occur for overpressures exceeding 4. With all other parameters held constant, that would imply that higher powered jets are inclined to break up and edge-darkened. However, the absolute power and radio galaxy morphology may well be related in the opposite sense (Massaglia et al. 2016), although no clear relationship exists (Mingo et al. 2019).

As proposed by Bicknell (1985), we suspect that the dependence on Mach number is crucial and a study of higher Mach number overpressured jets is first needed to complement the present Mach 2 results. In addition, jet power, density ratio, and the magnetization parameter are further important factors (Massaglia et al. 2022).

9 CONCLUSIONS

We have performed a systematic study of supersonic hydrodynamic jets injected into a lower pressure medium. As a first reference work, we take a Mach number of 2. These collimated circular jets, covering a range of densities and pressures, penetrate through a uniform ambient medium. This leaves behind distinctive flow patterns and shock configurations in the vicinity of the nozzle, which is the subject of the present investigation.

Our aims are to characterize and quantify these well-known flows through a large number of numerical simulations. This will serve as our basis for follow-up studies of high Mach number jets with pulsations, episodes, magnetic fields, etc. With this knowledge, we can interpret structures observed in a variety of man-made, natural, and astrophysical outflows.

The initial and boundary conditions should be noted. We do not begin with a pre-formed channel. Rather than an initial condition with a jet already stretching across the grid, we allow the jet to gently enter the medium, The ambient pressure may thus be altered although the presence of oscillations may well have more influence on the variations in the ambient pressure anyway. Tests to see if the initial jet ramping significantly alters the final state proved negative.

Stationary flow patterns are found to be rare but can be achieved out to the first shock for low overpressures, and approximated out to the third shock. This regime corresponds to regular reflection or diamond shock patterns, present out to overpressures of about 4.

At high overpressures, Mach reflection occurs in which a Mach shock disc intercepts the jet transversely. In all cases, the location of this shock front and the subsequent plume is strongly variable about the mean flow pattern. The variability is oscillatory with a period that depends on the density ratio.

We analyse the distance of the shock fronts from the nozzle along the axis. Oscillations in the stand-off distance are followed and used to determine mean shock positions and deviations.

For regular reflection at very low jet overpressures with Mach 2, the stand-off shock occurs at a distance along the axis of 1.82 - 1.84 jet radii as expected from theory. The second shock is located at an interval of ∼4.2 and the third shock at another ∼5.4, rather than being equally spaced.

We suspect that the oscillatory motions will drive sound waves far into the surroundings. However, the energy flux is generally towards the jet as the jet drags the immediate ambient gas out along the jet direction. This sets up vortices to circulate the material that re-enters laterally. Nevertheless, despite the vortices, sound waves can propagate laterally in a range of cases associated with light jets.

The oscillations generate noise called screech with typical quasi-oscillation times that can be estimated from the stand-off distance and the speed of surface waves through the Kelvin–Helmholtz instability. For the simulations presented here, the screech frequency is ~ 0.4–$0.6 c_{\rm amb}/R_{\rm jet}$ and ~ 0.12–$0.24 c_{\rm amb}/R_{\rm jet}$ for light and heavy jets, respectively. Thus, light jets induce higher frequency oscillations with a frequency of the order of 3.000 Hz for an exhaust of 10 diameter cm through the atmosphere. For a a jet emanating from a protostar and piercing through a core, this may be of the order of 10^{-10} Hz and for a radio galaxy jet exiting an inner bulge 10^{-15} Hz.

The location of the Mach disc follows the formula given by equation (4). This result can be understood by eliminating the Mach number to yield

$$D_1 = 1.38(\rho_{\rm jet} v_{\rm jet}^2 / p_{\rm amb})^{1/2}. \quad (13)$$

Remarkably, this shows that the stand-off distance depends only on the initial ram pressure at the nozzle and the ambient pressure. This is plausible when noting that the post-shock pressure at the Mach disc, after accounting for the expansion in the silent zone between the nozzle and disc, is roughly equal to the ambient pressure. The important point is that the jet expansion occurs with an opening angle inversely proportional to the Mach number while the expansion scalelength is also proportional to the Mach number since the expansion does not begin until a distance $D_i = \arcsin M$. Hence, the ram pressure at the Mach disc is simply inversely proportional to the distance squared. However, it should be noted that this is not a one-dimensional flow problem and a rigorous analysis is not tractable even employing characteristic methods.

The square-root behaviour is confirmed here for matched density and heavy jets (see Table 3. However, for light jets, we find that $D_1 \propto \kappa^{0.39}$. In fact, light jet simulations at high κ reveal non-uniform ambient pressure distributions as the moving Mach disc perturbs the ambient medium (see lower right-hand panel of Fig. 7.

There is some potential for an observed string of knots in a jet to yield useful physical information. While the separations are not sensitive to the density, both the Mach number and overpressure may be extractable. The Mach number dependence will be determined in a follow-up to this study.

The energy transport has been investigated. Along the axis, the total energy flux is conserved with regular exchange between kinetic and thermal/enthalpy. A small drop in the axial total energy flux for $\kappa = 2$ (middle panel of Fig. 12) is accounted for by a positive lateral flux for $\kappa = 2$ (middle panel of Fig. 13).

However, apart from a small range of low-density jets, the net flux of energy from the surroundings is towards the jet, radially inwards. Ambient gas is convected outwards and large vortices are induced. This flow is a result of the unsteady nature of the jet flows, which produces a constant exchange of momentum across the interface. The oscillations can still lead to some noise or sound waves escaping laterally but most of the time is consumed with the inward advection dominating.

Observations of strings of knots within astrophysical jets can provide multiple constraints (Reipurth, Raga & Heathcote 1992; Jorstad et al. 2005; Gómez et al. 2016; Derlopa et al. 2019). There are several obstacles in this regard that include the relationship between physical parameters and the radiation detected, the orientation, the physical jet radius and the density distribution in the ambient medium. In addition, where proper motions are measurable, it is usually found that the knots possess high-speed outward motions. Nevertheless, simulations can provide evidence for overpressured jets that undergo recollination (Fuentes et al. 2018).

There is efficient energy exchange in the regular reflection regime at low overpressures. Hence, the appearance of a string of knots would require a conversion mechanism that is effective across the fronts such as diffusive particle acceleration or the burning of excess fuel. On the other hand, Mach shock discs drastically change the jet downstream. According to the analysis, the pressure of the shocked gas is approximately equal to the ambient pressure. This may distinguish it from that of moving shocks stimulated by source outbursts that could nurture much higher pressures. We will return to this in a following work where we present virtual observations from these simulations.

Other factors make strong contributions to shock stability, For example, a magnetic field may provide a cushioning force when frozen in while C-shock instabilities may dominate when the field can diffuse through the gas. Also, cooling and chemistry can lead to unstable shock structures in a warm atomic and cool molecular flows. Shear, opening angle and ambient gradients will all complicate any interpretation.

There are examples of quasi-stationary shocks associated with jets, such as the protostellar jet HH154 (Favata et al. 2006) proposed to be a diamond shock (Bonito et al. 2011) and a fraction of blazars (Weaver et al. 2022). However, there is insufficient data to constrain individual jet properties.

DATA AVAILABILITY

No new observational data were generated or analysed in support of this research. Simulation source files are available on request. The data underlying this paper will be shared on reasonable request to the corresponding author.

REFERENCES

Adamson T., Jr, Nicholls J. A., 1959, J. Aerosp. Sci., 26, 16
Ahmane Z., Mignone A., Zanni C., Massaglia S., Bouldjderi A., 2020, Ap&SS, 365, 94
Bambic C. J., Reynolds C. S., 2019, ApJ, 886, 78
Barkov M. V., Bosch-Ramon V., 2022, MNRAS, 510, 3479

Bicknell G. V., 1985, PASA, 6, 130
Blake G. M., 1972, MNRAS, 156, 67
Blandford R. D., Rees M. J., 1974, MNRAS, 169, 395
Bonito R., Orlando S., Miceli M., Peres G., Micela G., Favata F., 2011, ApJ, 737, 54
Bourne M. A., Sijacki D., 2021, MNRAS, 506, 488
Buckley F. I. J., 1975, AIAA J., 13, 105
Buehrke T., Mundt R., Ray T. P., 1988, A&A, 200, 99
Carlson D. J., Lewis C. H., 1964, AIAA J., 2, 776
Davidor W., Penner S. S., 1971, AIAA J., 9, 1651
Daviller G., Dombard J., Staffelbach G., Herpe J., Saucereau D., 2020, Int. J. Comput. Fluid Dyn., 34, 622
Derlopa S., Akras S., Boumis P., Steffen W., 2019, MNRAS, 484, 3746
Dionatos O., Güdel M., 2017, A&A, 597, A64
Donohoe J., Smith M. D., 2016, MNRAS, 458, 558
Dubois Y., Devriendt J., Slyz A., Teyssier R., 2010, MNRAS, 409, 985
Ehlert K., Weinberger R., Pfrommer C., Springel V., 2021, MNRAS, 503, 1327
Ehlert K., Weinberger R., Pfrommer C., Pakmor R., Springel V., 2022, preprint (arXiv:2204.01765)
Fabian A. C., 2012, ARA&A, 50, 455
Falceta-Gonçalves D., Caproni A., Abraham Z., Teixeira D. M., de Gouveia Dal Pino E. M., 2010, ApJ, 713, L74
Fanaroff B. L., Riley J. M., 1974, MNRAS, 167, 31P
Favata F., Bonito R., Micela G., Fridlund M., Orlando S., Sciortino S., Peres G., 2006, A&A, 450, L17
Franquet E., Perrier V., Gibout S., Bruel P., 2015, Prog. Aerosp. Sci., 77, 25
Fuentes A., Gómez J. L., Martí J. M., Perucho M., 2018, ApJ, 860, 121
Gao J. H., Li X. D., 2010, J. Acoust. Soc. Am., 127, 1251
Gómez J. L., Martí J. M., Marscher A. P., Ibáñez J. M., Alberdi A., 1997, ApJ, 482, L33
Gómez J. L. et al., 2016, ApJ, 817, 96
Hansen C. J. et al., 2008, Nature, 456, 477
Hardcastle M. J., Krause M. G. H., 2013, MNRAS, 430, 174
Hardee P. E., 1979, ApJ, 234, 47
Heinrich A. M., Chen Y.-H., Heinz S., Zhuravleva I., Churazov E., 2021, MNRAS, 505, 4646
Hillel S., Soker N., 2017, MNRAS, 466, L39
Huško F., Lacey C. G., 2022, preprint (arXiv:2205.08884)
Jorstad S. G. et al., 2005, AJ, 130, 1418
Kirkpatrick C. C., McNamara B. R., 2015, MNRAS, 452, 4361
Knee L. B. G., Sandell G., 2000, A&A, 361, 671
Liger-Belair G., Cordier D., Georges R., 2019, Sci. Adv., 5, eaav5528
Lubert C. P., 2017, J. Acoust. Soc. Am., 142, 2489
Martí J. M., Perucho M., Gómez J. L., 2016, ApJ, 831, 163
Martí J.-M., 2019, Galaxies, 7, 24
Martizzi D., Quataert E., Faucher-Giguère C.-A., Fielding D., 2019, MNRAS, 483, 2465
Massaglia S., Bodo G., Rossi P., Capetti S., Mignone A., 2016, A&A, 596, A12
Massaglia S., Bodo G., Rossi P., Capetti A., Mignone A., 2022, A&A, 659, A139
Massi F., López R., Beltrán M. T., Estalella R., Girart J. M., 2022, A&A, 664, A11
Meyer E. T. et al., 2016, Science, 15, 100.01
Mignone A., Bodo G., Massaglia S., Matsakos T., Tesileanu O., Zanni C., Ferrari A., 2007, ApJS, 170, 228
Mingo B. et al., 2019, MNRAS, 488, 2701
Mizuno Y., Gómez J. L., Nishikawa K.-I., Meli A., Hardee P. E., Rezzolla L., 2015, ApJ, 809, 38
Moya-Torregrosa I., Fuentes A., Martí J. M., Gómez J. L., Perucho M., 2021, A&A, 650, A60
Norman M. L., Winkler K.-H. A., Smarr L., Smith M. D., 1982, A&A, 113, 285
Ogden D. E., Wohletz K. H., Glatzmaier G. A., Brodsky E. E., 2008, J. Geophys. Res., 113, B02204
Perlman E. S., Biretta J. A., Sparks W. B., Macchetto F. D., Leahy J. P., 2001, ApJ, 551, 206
Porth O., Komissarov S. S., 2015, MNRAS, 452, 1089
Powell A., 1953, Proc. Phys. Soc. B, 66, 1039
Prasad D., Voit G. M., O'Shea B. W., 2022, ApJ, 932, 18
Reipurth B., Raga A. C., Heathcote S., 1992, ApJ, 392, 145
Reynolds C. S., Balbus S. A., Schekochihin A. A., 2015, ApJ, 815, 41
Sanders R. H., 1983, ApJ, 266, 73
Smith M. D., 1982, ApJ, 259, 522
Smith M. D., 2012, Astrophys. Jets Beams. Cambridge University Press, Cambridge
Smith M. D., Donohoe J., 2019, MNRAS, 490, 1363
Smith M. D., Donohoe J., 2021, MNRAS, 502, 423
Smith M. D., O'Connell B., Davis C. J., 2007, A&A, 466, 565
Tam C. K. W., 1995, Annu. Rev. Fluid Mech., 27, 17
Toro E. F., Spruce M., Speares W., 1994, Shock Waves, 4, 25
Tran K., Lim D., Min S., Mavris D., 2018, AIAA, 2018, 2816
Vincent J. B. et al., 2016, MNRAS, 462, S184
Weaver Z. R. et al., 2022, APJS, 260, id.12
Weinberger R., Ehlert K., Pfrommer C., Pakmor R., Springel V., 2017, MNRAS, 470, 4530
Yang H. Y. K., Reynolds C. S., 2016, ApJ, 829, 90

APPENDIX A: ANALYTICAL FORMULAS

The mass flux injected on to the domain is

$$\dot{\mathcal{M}}_{\rm jet} = \rho_{\rm jet} \times v_{\rm jet} \times A, \tag{A1}$$

where $A = (1-\mu)\pi R_{\rm jet}^2$ is the jet area. Here, μ represents a small adjustment since the numerical nozzle profile is an approximation to a circle of radius $R_{\rm jet}$. There will be a linear increase with time for all the simulations with reflective outflow boundaries because the mass influx is constant throughout the present set of simulations. With an outflow boundary condition, the cocoon back flow removes mass from the grid, as discussed below. In terms of the scaling, $\dot{\mathcal{M}}_{\rm jet} = (1-\mu)(\pi\gamma\kappa\eta)^{1/2}M$.

The momentum flow rate on to the grid is

$$P = (\rho_{\rm jet} \times v_{\rm jet}^2 + p_{\rm jet}) \times A. \tag{A2}$$

This can be written in the non-dimensional form

$$P = \pi\kappa(\gamma M^2 + 1). \tag{A3}$$

Finally, the energy flux has two components: the kinetic flux and the enthalpy flux, which, in turn, consists of the internal energy and the work done, $p\mathcal{V}$, where $\mathcal{V} = 1/\rho$ is the specific volume. On dividing through by the mass conservation relation, this simplifies to Bernoulli's equation with the Bernoulli constant, U:

$$\mathrm{U}^2 = v_{\rm jet}^2 + \frac{2\gamma}{\gamma-1}\frac{p_{\rm jet}}{\rho_{\rm jet}}. \tag{A4}$$

Therefore, the total available power entering the domain is $\dot{\mathcal{M}}_{\rm jet}\mathrm{U}^2/2$. We can also follow the equivalent quantities downstream to understand how energy is exchanged between forms and media.

Although the equation of state is adiabatic and the shocks are termed adiabatic, the adiabat changes across a shock front. Hence, we expect the total entropy flux to decrease with distance from the nozzle, although any back-flow may negate this. The entropy increase in the jet can be found by integrating over all jet zones the quantity

$$\mathrm{S} - \mathrm{S_o} = C_V \rho \ln\left[(p/p_{\rm jet}) - \gamma(\rho/(\rho_{\rm jet})\right]. \tag{A5}$$

Several different time-scales are relevant. The time-scale for the propagation of the jet head across the grid can be derived from a steady working surface model. This assumes that the jet ploughs into the ambient medium with the interface advancing at a speed, V. A high-pressure hotspot is produced by the shocked jet and is

approximately balanced by the pressure of the shocked ambient medium. We thus need to employ the jump shock relationships that apply in the frame of the shock front. The pressure jump is given by

$$\frac{p_2}{p_1} = \frac{2\gamma}{\gamma+1}(M_s^2 - 1), \tag{A6}$$

where the Mach number M_s corresponds to the oncoming jet speed relative to the advance speed, which is $v_{jet} - V$. As a result, pressure equilibrium yields

$$\eta(v_{jet} - V)^2 - c_{jet}^2) = V^2 - c_{amb}^2. \tag{A7}$$

Manipulation yields estimate for the advance speed that applies for both light and heavy jets provided both shocks are strong:

$$V = v_{jet}\frac{\sqrt{\eta}}{1+\sqrt{\eta}}, \tag{A8}$$

which is remarkably independent of the overpressure when written in this form. However, in our parameter study, the jet Mach number is held constant and determines the structure within the jet. We thus rewrite this formula as

$$V = M\frac{\sqrt{\kappa}}{1+\sqrt{\eta}}. \tag{A9}$$

The actual propagation time, however, was found to be lower than the above theoretical value even for a pressure-matched jet (Donohoe & Smith 2016). One needs to include a drag coefficient that takes into account the gradual opening of the jet, the full area presented as the jet flow is turned into the cocoon and the deflection of the ambient medium. In addition, a feedback loop results in an oscillation of the interface with vortices rolling back from the interface and squeezing the upstream jet. Furthermore, the expansion due to the initial high jet pressures considered here will increase the mean jet radius and thus slow the propagation.

This paper has been typeset from a TEX/LATEX file prepared by the author.